Journal of Alloys and Compounds 823 (2020) 153807

Contents lists available at ScienceDirect

Journal of Alloys and Compounds

journal homepage: http://www.elsevier.com/locate/jalcom

An orthorhombic $D0_{22}$-like precursor to Al_8Mo_3 in the Al—Mo—Ti system

A. Leineweber [a, *], M.J. Kriegel [a], B. Distl [a, 1], S. Martin [a], V. Klemm [a], S.-L. Shang [b], Z.-K. Liu [b]

[a] Institute of Materials Science, TU Bergakademie Freiberg, 09599, Freiberg, Germany
[b] Department of Materials Science and Engineering, The Pennsylvania State University, University Park, PA, 16802, USA

ARTICLE INFO

Article history:
Received 17 October 2019
Received in revised form
7 January 2020
Accepted 9 January 2020
Available online 15 January 2020

Keywords:
Intermetallics (aluminides
Silicides)
Crystal chemistry
Phase transformation (crystallographic aspects kinetics and mechanisms)
Microstructure
Ab-initio calculations
X-ray diffraction
Transmission Kikuchi diffraction

ABSTRACT

A peculiar checkerboard microstructure has been observed in as-cast Mo-rich Al—Mo—Ti alloys with slightly less than 75 at.% Al. It contains a Mo-rich tetragonal $D0_{22}$-Al_3Ti phase as well as an orthorhombically distorted variant thereof, with a somewhat higher Mo content, referred to as $D0_{22}$'. Both phases are fcc-based superstructures originating mainly from ordering of transition metal (*TM*) vs. Al. The measured lattice parameters of the $D0_{22}$' phase were evaluated using strain tensors quantifying the strain with respect to some average fcc substructure. Thereby, it was shown that the $D0_{22}$' structure possesses some common features with the binary Al_8Mo_3 and Al_3Mo fcc-based superstructures known from the Al—Mo system. It is made likely that $D0_{22}$' as well as Al_8Mo_3 and Al_3Mo (with Mo being a group-vi transition metal) are some continuation of the series of structures observed for Al_3TM with *TM* from group iii via iv to v with increasing average number of electrons per atom. This view is supported by first-principles calculations which indicate elastic instability of a hypothetical $D0_{22}$-Al_3Mo structure towards an orthorhombically distorted structure.

The checkerboard microstructure likely forms directly after solidification from a homogeneous $D0_{22}$ structure by decomposition into Mo-richer ($D0_{22}$') and -poorer regions. The phase interface orientations can be reconciled with the deformation necessary to transform $D0_{22}$ into $D0_{22}$'. Further annealing at elevated temperatures leads to decomposition of the microstructures, resulting in formation of Al_8Mo_3 and Mo-depleted $D0_{22}$, indicating that the $D0_{22}$' phase is metastable.

1. Introduction

Intermetallic phases based on the Al—Ti binary system attract a lot of interest as phase constituents of various types of alloys for structural applications, in particular, for high-strength high-temperature purposes like the γ-AlTi-base alloys [1]. Interest also exists in application of the Al_3Ti phase, which exhibits a density even lower than that of γ-AlTi. The ($D0_{22}$-)Al_3Ti phase, however, suffers from high brittleness, which is attributed to its tetragonal $D0_{22}$ fcc[2]-base superstructure (see Fig. 1, but also see below). An idea to cope with this brittleness is to substitute either Al or Ti by some other elements, transforming the tetragonal-$D0_{22}$-type (super)structure into the cubic $L1_2$ superstructure [2,3], which is supposed to reduce brittleness and to improve deformability due to an increased number of slip systems.

The structural trends observed upon alloying of Al_3Ti can be rationalized based on the development of the fcc-based crystal structures of the group-iii to group-v transition metal (*TM*) trialuminides with increasing group number, i.e., with increasing average number of electrons per atom (*e*/*at*) in Al_3TM (see Fig. 1). The $L1_2$ structure is adopted by fcc-based group-iii transitions trialuminides (Al_3Sc, Al_3Lu and as well as some other late lanthanides with 10.50 *e*/*at*; Al_3Y and other further lanthanides form polytypes involving hexagonal stacking [4]). The group-iv trialuminides Al_3Zr and Al_3Hf (*e*/*at* = 10.75) are usually reported to exhibit the tetragonal $D0_{23}$ superstructure [5,6], whereas, as mentioned before, the homologous Al_3Ti is usually observed to adopt the tetragonal $D0_{22}$ superstructure [5]. First-principles calculations using density functional theory (DFT), however, reveal, that — at least at 0 K — $D0_{23}$-Al_3Ti should have a lower energy than $D0_{22}$-Al_3Ti, in accordance with the structures of Al_3Zr and Al_3Hf [7—9]. In fact, low-temperature polymorphs of Al_3Ti intermediate between $D0_{22}$ and

* Corresponding author.
E-mail address: andreas.leineweber@iww.tu-freiberg.de (A. Leineweber).
[1] present address: Max-Planck-Institut für Eisenforschung GmbH, Postfach 140444, D-40074 Düsseldorf, Germany.
[2] As it is common practice the term face-centred cubic (fcc), for which it might make sense to reserve it to denote a Bravais lattice, is used to denote the cubic closed packed structure.

https://doi.org/10.1016/j.jallcom.2020.153807
0925-8388/

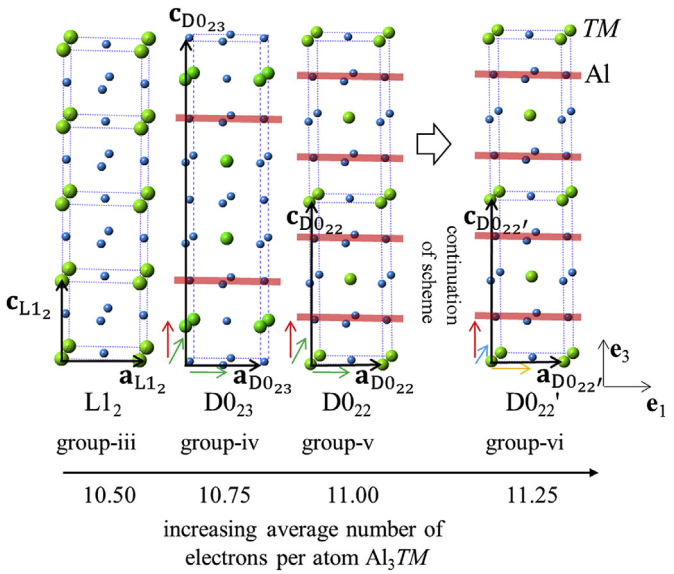

Fig. 1. Clinographic view of the cubic $L1_2$, tetragonal $D0_{23}$ and $D0_{22}$ fcc superstructures (S) occurring according to Refs. [14–18] with increasing number of electrons per atom for early-transition metal (*TM*) trialuminides. Horizontal thick bars indicate antiphase boundaries with respect to $L1_2$. The Cartesian basis vectors $\mathbf{e}_1$–$\mathbf{e}_3$ adopted for strain analysis (see section 3.1) point along $[100]_S$, $[010]_S$ and $[001]_S$. In the tetragonal cases ($D0_{23}$ and $D0_{22}$) green and red arrows indicate the directions of the eigenvectors of the spontaneous strain tensor ε_{Aizu} pertaining to the sorted eigenvalues ($-s$, $-s$, $2s$ with positive s), as it is done for the orthorhombic $D0_{22}$' case by blue, yellow and red vectors (approximate eigenvalues $-s$, 0, $+s$). (For interpretation of the references to color in this figure legend, the reader is referred to the Web version of this article.)

$D0_{23}$ have been reported [10,11]. In line with this, similar polymorphism seems to exist also for Al_3Hf [12]. Group-v transition metal aluminides Al_3V, Al_3Nb and Al_3Ta ($e/at = 11.00$) are all found to exhibit the $D0_{22}$ structure [5,13]. The $D0_{23}$ and $D0_{22}$ structures can be regarded as related to the $L1_2$ structure by introducing antiphase boundaries on one set of $\{001\}_{fcc}$ planes highlighted by red lines in Fig. 1. The index fcc denotes that crystallographic quantities, here lattice plane orientations, refer to conventional unit cell of the fcc basis structure underlying all superstructures discussed in the present work. The procedure is analogous, if crystallographic quantities refer to superstructures.

This observed and theoretically predicted structural transition for Al_3TM from $L1_2$ via $D0_{23}$ to $D0_{22}$ with increasing average e/at has been attributed to a structure-dependent density of states, which is filled by the electrons per atom provided by the constituting atoms [14–18]. Substitution of either the *TM* or Al in various *TM* trialuminides by other *TM* or main-group elements can then also be regarded as a change of the average e/at which drives structural change. For example, substitution of Al by Zn, Cu, Ni reduces the number of electrons (per atom) whereas substitution of Ti by Nb and Mo increases the average e/at.

An easy continuation of the $L1_2$ via $D0_{23}$ to $D0_{22}$ scheme shown in Fig. 1 for binary group-iii to group-v *TM* trialuminides from beyond group v has not been developed until now. Group-vi *TM*–Al intermetallics forming a fcc superstructure close to 75 at.% Al, however, are known: Al_8Mo_3 and *exp*-Al_3Mo[3] [19,20]; see Fig. 2[4] Both superstructures are more complex than those of the group-iii to group-v *TM* trialuminides. A recently developed electron-counting scheme to predict stability of *TM*–main group metal intermetallics, involving considerations on the number of the 1st and 2nd nearest-neighbor *TM*–*TM* pairs, covers the $L1_2$ via $D0_{23}$ to $D0_{22}$ transition and was also found to be compatible with atomic ordering of Al_8Mo_3 [18]. *exp*-Al_3Mo, however, has not been included into discussion of the proposed electron counting rules.

In the present work the occurrence of an orthorhombically distorted $D0_{22}$ variant ($D0_{22}$') in as-cast ternary Al–Mo–Ti alloys is reported. That structure was always found to coexist with the undistorted tetragonal $D0_{22}$ phase in some kind of checkerboard microstructure. By analyzing the distortion of the unit cell metric of the orthorhombic structure away from a pseudocubic fcc one by means of special strain tensors, it is shown that the $D0_{22}$' structure shares common structural characteristics with the structure of *exp*-Al_3Mo and, in particular, Al_8Mo_3. It is suggested that the $D0_{22}$' structure developed after unmixing of $D0_{22}$, which has formed upon solidification, into Mo-rich and Mo-poor regions. The Mo-rich regions have a composition already close to Al_8Mo_3 which forms after prolonged annealing alongside with Mo-depleted $D0_{22}$ phase in agreement with the results in the literature [23–25].

2. Methods

2.1. Alloy preparation

The $D0_{22}$' structure was observed on a series of as-cast Al–Mo–Ti alloys, some of which were already used in previous studies [23,26]. The nominal compositions will be indicated in the form of a formula $Al_nMo_mTi_o$ with *n, m* and *o* indicating the Al, Mo and Ti contents in at.% (see Table 1). Starting materials for alloy preparation were powders of Al and Ti (99.5%, MaTeck GmbH, Germany) as well as Mo (99.9%, Plansee SE, Austria). In order to reduce surface contamination by oxidation, the Mo powder was heat-treated at 700 °C for 14 h in hydrogen atmosphere, prior further use. The powders were mixed in conventional mills and afterwards pressed to tablets using a load of >500 MPa. These tablets were melted by arc-melting (Edmund Buehler GmbH, Germany) on a water-cooled copper mold. In order to achieve a good homogeneity, the samples were turned-over and re-melted several times. The as-cast alloys discussed in the present paper result from this melting procedure. A single alloy ($Al_{73}Mo_{22}Ti_5$) was further heat treated under flowing Ar in a vertical tube furnace for 12 h at 1400 °C followed by quenching in ice water.

The average chemical compositions of the alloys were controlled by electron probe micro analysis using wavelength dispersive X-ray spectroscopy (JEOL JXA-8230 Superprobe, Japan). Only slight deviations from the nominal composition were detected.

2.2. Analysis of atomic structure and of microstructure

Powder X-ray diffraction (PXRD) analysis was performed based on the data recorded on a Bruker D8 Advance (Bruker AXS) Bragg-Brentano type diffractometer equipped with a sealed X-ray tube with Co anode. The primary beam was monochromatised by a SiO_2 Johannsson-type monochromator to eliminate all radiation components except Co-Kα_1 (wave length 1.78897 Å). The diffracted beam was recorded by a LynxEye 1D detector after passing a Soller collimator with 0.25° acceptance. The patterns were recorded from pulverized alloy sedimented on a (510)-cut "zero background" Si wafer. Data were recorded in an angular range of $2\theta = 15\ldots160°$ with a step size of ≈0.01°.

Whole powder pattern based refinements were employed applying the Rietveld method within the TOPAS [27,28] software package to verify the phase compositions and to determine the

[3] In the present paper the experimentally encountered crystal structure of Al_3Mo will be referred to as *exp*-Al_3Mo due to the use of the Al_3Mo for a couple of further structures of the same composition. If the formula Al_3Mo appears without a phase label, simply the composition by this formula is implied.

[4] A single report exists for a $D0_{22}$-like structure having developed upon annealing ball-milled $Al_{75}Mo_{25}$ [22].

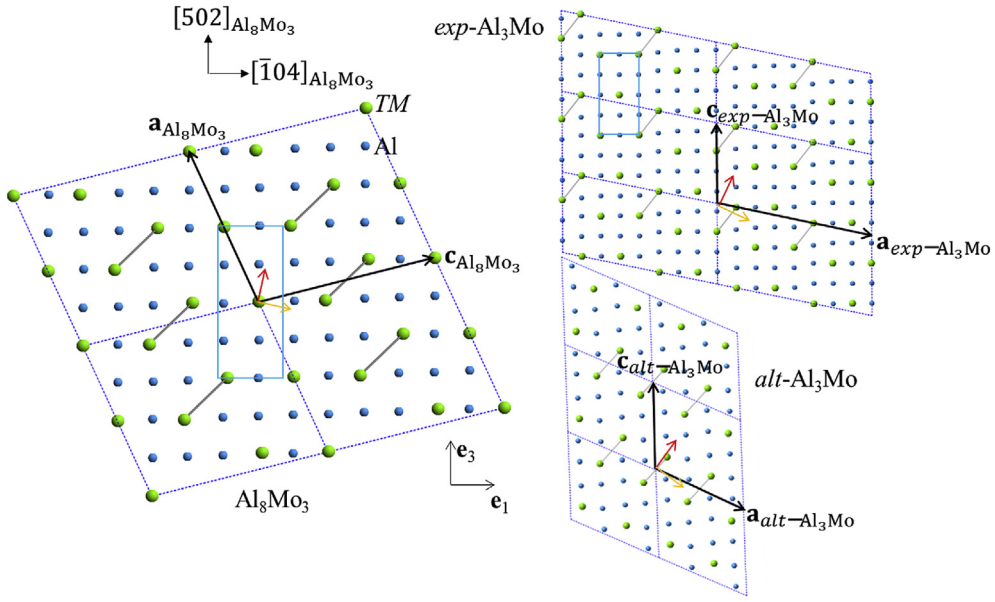

Fig. 2. Fcc based superstructures (*S*) experimentally encountered for Al_8Mo_3 (left, space group *C*2/*m* [19,20]) and Al_3Mo (*exp*-Al_3Mo; top right, *Cm* description [21], not considering the likely presence of inversion centers, e.g. halfway between the pairs of Mo atoms), as well as hypothetical structure of an *alternative alt*-Al_3Mo, projected along $[010]_S$, respectively. Black arrows indicate the directions of Cartesian basis vectors $\mathbf{e}_1$ and $\mathbf{e}_3$ used to express the spontaneous strain ε_{Aizu}. Yellow and red arrows indicate the directions of the eigenvectors of ε_{Aizu} pertaining to the $-s$, 0 and $+s$ eigenvalues given in Table 2. Note that atoms alternately occur at heights differing by $\mathbf{b}_S/2$ ($\mathbf{b}_{Al_8Mo_3}$, $\mathbf{b}_{exp\text{-}Al_3Mo}$, $\mathbf{b}_{alt\text{-}Al_3Mo}$). "Bonds" between Mo atoms highlight Mo–Mo 1st-n.n. pairs of a distance of 3.2–3.4 Å which constitute Mo–Mo first-neighbor pairs on the underlying fcc substructure. (For interpretation of the references to color in this figure legend, the reader is referred to the Web version of this article.)

Table 1
Al–Mo–Ti alloys considered in the present study. The nominal compositions (indices in atomic %) used in the text to refer to these alloys are calculated from the weighted-in portions. The table also contains the results from powder X-ray diffraction (PXRD) and EPMA analysis. Numbers in parentheses indicate standard deviations from Rietveld refinement.

Alloy; nominal composition	PXRD		EPMA	
	Mass fractions[a] of phases according to Rietveld refinement	Lattice parameters (Å, °)[b]	Alloy composition	Composition of $D0_{22}$ + $D0_{22}$' regions
$Al_{73}Mo_{22}Ti_5$ as-cast	$D0_{22}$ 0.553(3)	3.81129(5) 8.38216(14)	$Al_{71.6}Mo_{23.0}Ti_{5.4}$	$Al_{72.2}Mo_{24.3}Ti_{3.5}$
	$D0_{22}$' 0.447(3)	3.97762(9) 3.62953(7) 8.38492(13)		
$Al_{73}Mo_{22}Ti_5$ 1400 °C	$D0_{22}$ 0.721(7)[c]	3.8087(2) 8.3812(3)	$Al_{71.6}Mo_{23.3}Ti_{5.1}$	-
	Al_8Mo_3 0.279(3)	9.2135(5) 3.6405(2) 10.8842(5) 100.922(4)		
$Al_{74}Mo_{21}Ti_5$ as-cast	$D0_{22}$ 0.687(3)	3.80947(5) 8.39028(11)	$Al_{72.9}Mo_{21.9}Ti_{5.2}$	$Al_{72.9}Mo_{23.6}Ti_{3.5}$
	$D0_{22}$' 0.312(3)	3.96400(14) 3.63659(12) 8.3952(4)		
$Al_{70}Mo_{24}Ti_6$ as-cast	$D0_{22}$ 0.337(3)	3.81514(8) 8.37627(14)	$Al_{69.1}Mo_{24.4}Ti_{6.5}$	$Al_{71.8}Mo_{23.9}Ti_{4.3}$
	$D0_{22}$' 0.334(3)	3.99036(11) 3.62408(10) 8.37627(14)		
	Al_8Mo_3 0.274(2)	9.2196(3) 3.63346(10) 10.1365(3) 101.230(3)		
	bcc (~AlMo) 0.0547(9)	3.14842(10)		

[a] Due to the uncertain real distribution of the atom types (Al, Ti, Mo) on the different sites of some phases, the refined mass fractions for the various phases may suffer from systematic errors (see section 3.1).
[b] Given for the phases listed in the adjacent column as $D0_{22}$: $a_{D0_{22}}$ and $c_{D0_{22}}$; $D0_{22}$': $a_{D0_{22}'}$, $b_{D0_{22}'}$ and $c_{D0_{22}'}$; Al_8Mo_3: $a_{Al_8Mo_3}$, $b_{Al_8Mo_3}$, $c_{Al_8Mo_3}$ and $\beta_{Al_8Mo_3}$.
[c] Traces of reflections from $D0_{22}$' appear visible, which, however, have not been included into the Rietveld refinement.

Table 2
Lattice metrics of fcc based superstructures in the Al–Mo–Ti system and of further such superstructures used for comparison analyzed in terms of the spontaneous strain ε_{Aizu} according to Ref. [44] analyzed in terms of eigenvalues and eigenvectors and x_s according to Eq. (4).

Phase	Space group, Point group	A^T in Eq. (2b) [c]	Superstructure cell axial ratio for tetragonal structures	Spontaneous strain ε_{Aizu}	sorted eigenvalues of ε_{Aizu}	column vectors of eigenvectors in sequence of eigenvalues	Spontaneous strain measure x_s
Literature; experimental							
$L1_2$-Al_3Sc [4]	$Pm\bar{3}m$, $m\bar{3}m$	$\begin{pmatrix}1&0&0\\0&1&0\\0&0&1\end{pmatrix}$	$a_{L1_2} = 4.103$ Å ($c_{L1_2}/a_{L1_2} = 1$)	$\begin{pmatrix}0&0&0\\0&0&0\\0&0&0\end{pmatrix}$	0 0 0	$\begin{pmatrix}1&0&0\\0&1&0\\0&0&1\end{pmatrix}$	(0)
$D0_{22}$-Al_3Ti [46]	$I4/mmm$, $4/mmm$	$\begin{pmatrix}1&0&0\\0&1&0\\0&0&2\end{pmatrix}$	$a_{D0_{22}} = 3.8537$ Å $c_{D0_{22}} = 8.5838$ Å $c_{D0_{22}}/(2a_{D0_{22}}) = 1.114$	$\begin{pmatrix}-.037&0&0\\0&-.037&0\\0&0&.073\end{pmatrix}$	$-0.037 = -s$ $-0.037 = -s$ $+0.073 = 2s$	$\begin{pmatrix}1&0&0\\0&1&0\\0&0&1\end{pmatrix}$	0.089
$D0_{23}$-Al_3Zr [47]	$I4/mmm$, $4/mmm$	$\begin{pmatrix}1&0&0\\0&1&0\\0&0&4\end{pmatrix}$	$a_{D0_{23}} = 3.9993$ Å $c_{D0_{23}} = 17.283$ Å $c_{D0_{23}}/(4a_{D0_{23}}) = 1.080$	$\begin{pmatrix}-.0261&0&0\\0&-.0261&0\\0&0&.0522\end{pmatrix}$	$-0.026 = -s$ $-0.026 = -s$ $+0.052 = 2s$	$\begin{pmatrix}1&0&0\\0&1&0\\0&0&1\end{pmatrix}$	0.064
$D0_{22}$-Al_3Nb [48]	$I4/mmm$, $4/mmm$	$\begin{pmatrix}1&0&0\\0&1&0\\0&0&2\end{pmatrix}$	$a_{D0_{22}} = 3.841$ Å $c_{D0_{22}} = 8.609$ Å $c_{D0_{22}}/(2a_{D0_{22}}) = 1.121$	$\begin{pmatrix}-.039&0&0\\0&-.039&0\\0&0&.077\end{pmatrix}$	$-0.039 = -s$ $-0.039 = -s$ $+0.077 = 2s$	$\begin{pmatrix}1&0&0\\0&1&0\\0&0&1\end{pmatrix}$	0.095
Al_8Mo_3 [19] [b]	$C2/m$, $2/m$	$\begin{pmatrix}-1&0&2.5\\0&-1&0\\2&0&0.5\end{pmatrix}$	$a_{Al_8Mo_3} = 9.208$ Å $b_{Al_8Mo_3} = 3.6378$ Å $c_{Al_8Mo_3} = 10.065$ Å $\beta_{Al_8Mo_3} = 100.78°$	$\begin{pmatrix}.080&0&.019\\0&-.074&0\\.019&0&.006\end{pmatrix}$	$-0.074 \approx -s$ $-0.010 \approx 0$ $+0.084 \approx s$	$\begin{pmatrix}0&.978&.208\\-1&0&0\\0&-.208&.978\end{pmatrix}$	0.112
exp-Al_3Mo [21]	$C2/m$ [a], $2/m$	$\begin{pmatrix}4&0&0\\0&1&0\\-1&0&2\end{pmatrix}$	$a_{exp\text{-}Al_3Mo} = 16.396$ Å $b_{exp\text{-}Al_3Mo} = 3.594$ Å $c_{exp\text{-}Al_3Mo} = 8.386$ Å $\beta_{exp\text{-}Al_3Mo} = 101.88°$	$\begin{pmatrix}.021&0&.027\\0&-.086&0\\.027&0&.066\end{pmatrix}$	$-0.087 \approx -s$ $+0.003 \approx 0$ $+0.084 \approx s$	$\begin{pmatrix}0&.855&.518\\-1&0&0\\0&-.518&.855\end{pmatrix}$	0.117
This work; experimental; from as-cast $Al_{73}Mo_{22}Ti_5$							
$D0_{22}$-Al_3(Ti,Mo)	$I4/mmm$, 4/mmm	$\begin{pmatrix}1&0&0\\0&1&0\\0&0&2\end{pmatrix}$	$a_{D0_{22}} = 3.811$ Å $c_{D0_{22}} = 8.382$ Å $c_{D0_{22}}/(2a_{D0_{22}}) = 1.100$	$\begin{pmatrix}-.032&0&0\\0&-.032&0\\0&0&.064\end{pmatrix}$	$-0.032 = -s$ $-0.032 = -s$ $+0.064 = 2s$	$\begin{pmatrix}1&0&0\\0&1&0\\0&0&1\end{pmatrix}$	0.079
$D0_{22}'$-Al_3(Ti,Mo)	$Immm$, mmm	$\begin{pmatrix}1&0&0\\0&1&0\\0&0&2\end{pmatrix}$	$a_{D0_{22}'} = 3.978$ Å $b_{D0_{22}'} = 3.629$ Å $c_{D0_{22}'} = 8.385$ Å	$\begin{pmatrix}.012&0&0\\0&-.077&0\\0&0&.065\end{pmatrix}$	$-0.074 \approx -s$ $-0.010 \approx 0$ $+0.084 \approx s$	$\begin{pmatrix}0&1&0\\-1&0&0\\0&0&1\end{pmatrix}$	0.101
This work, first-principles calculations							
$L1_2$-Al_3Mo	$Pm\bar{3}m$, $m\bar{3}m$	$\begin{pmatrix}1&0&0\\0&1&0\\0&0&1\end{pmatrix}$	$a_{L1_2} = 3.926$ Å ($c_{L1_2}/a_{L1_2} = 1$)	$\begin{pmatrix}0&0&0\\0&0&0\\0&0&0\end{pmatrix}$	0 0 0	$\begin{pmatrix}1&0&0\\0&1&0\\0&0&1\end{pmatrix}$	(0)
$L1_2$'-Al_3Mo	$P4/mmm$, $4/mmm$	$\begin{pmatrix}1&0&0\\0&1&0\\0&0&1\end{pmatrix}$	$a_{L1_2'} = 3.783$ Å $c_{L1_2'} = 4.244$ Å $c_{L1_2'}/a_{L1_2'} = 1.122$	$\begin{pmatrix}-.039&0&0\\0&-.039&0\\0&0&.078\end{pmatrix}$	$-0.039 = -s$ $-0.039 = -s$ $+0.078 = 2s$	$\begin{pmatrix}1&0&0\\0&1&0\\0&0&1\end{pmatrix}$	0.097
$D0_{22}$-Al_3Mo	$I4/mmm$, $4/mmm$	$\begin{pmatrix}1&0&0\\0&1&0\\0&0&2\end{pmatrix}$	$a_{D0_{22}} = 3.806$ Å $c_{D0_{22}} = 8.386$ Å $c_{D0_{22}}/(2a_{D0_{22}}) = 1.102$	$\begin{pmatrix}-.033&0&0\\0&-.033&0\\0&0&.0668\end{pmatrix}$	$-0.0365 = -s$ $-0.0365 = -s$ $+0.0730 = 2s$	$\begin{pmatrix}1&0&0\\0&1&0\\0&0&1\end{pmatrix}$	0.080
$D0_{22}'$-Al_3Mo	$Immm$, mmm	$\begin{pmatrix}1&0&0\\0&1&0\\0&0&2\end{pmatrix}$	$a_{D0_{22}'} = 3.984$ Å $b_{D0_{22}'} = 3.647$ Å $c_{D0_{22}'} = 8.361$ Å	$\begin{pmatrix}.012&0&0\\0&-.074&0\\0&0&.062\end{pmatrix}$	$-0.074 \approx -s$ $-0.012 \approx 0$ $+0.062 \approx s$	$\begin{pmatrix}0&1&0\\-1&0&0\\0&0&1\end{pmatrix}$	0.097
exp-Al_3Mo	$C2/m$, $2/m$	$\begin{pmatrix}4&0&0\\0&1&0\\-1&0&2\end{pmatrix}$	$a_{Al_3Mo} = 16.463$ Å $b_{Al_3Mo} = 3.607$ Å $c_{Al_3Mo} = 8.403$ Å $\beta_{Al_3Mo} = 101.88°$	$\begin{pmatrix}.022&0&.026\\0&-.086&0\\.026&0&.064\end{pmatrix}$	$-0.086 \approx -s$ $-0.009 \approx 0$ $+0.077 \approx s$	$\begin{pmatrix}0&.813&.581\\-1&0&0\\0&-.581&.814\end{pmatrix}$	0.116
alt-Al_3Mo	$C2/m$, $2/m$	$\begin{pmatrix}2&0&0\\0&1&0\\-1&0&2\end{pmatrix}$	$a_{Al_3Mo} = 9.164$ Å $b_{Al_3Mo} = 3.555$ Å $c_{Al_3Mo} = 8.364$ Å $\beta_{Al_3Mo} = 115.90°$	$\begin{pmatrix}.046&0&.016\\0&-.102&0\\.016&0&.056\end{pmatrix}$	$-0.102 \approx -s$ $+0.034 \approx 0$ $+0.068 \approx s$	$\begin{pmatrix}0&.814&.581\\-1&0&0\\0&-.581&.814\end{pmatrix}$	0.127

[a] Originally given as *Cm*. Visual inspection of the crystal structure, however, suggests that the given structure model is well compatibly with presence of an inversion centre, leading to the symmetry *C2/m*. The same conclusion has been drawn based on the present first-principles calculations as well as in the literature (https://materialsproject.org/materials/mp-571247 [49]).
[b] Powder diffraction data from that work.
[c] For the monoclinic case $\mathbf{A}^T$ has been adapted in such a way that the orientation of ε and its eigenvectors eases comparison.

lattice parameters of present phases. The background was described by a 4th order Chebychev polynomial. Instrumental line broadening was assessed on the basis of diffraction data from LaB_6 660b NIST standard powder by fitting parameters using a variant of the pseudo-Voigt function [29]. Corresponding parameters were held fixed and parameters accounting for isotropic or anisotropic microstrain broadening as described in Refs. [27,30] were refined to account for the additional line broadening exhibited by different metallic phases.

The spatial distribution of individual phases was obtained from the scanning electron micrographs. These micrographs were taken using back-scattered electrons (SEM/BSE) with a FEG-SEM LEO 1530 GEMINI operating at 20 kV. Higher-resolution microstructure and atomic structure information were obtained by transmission electron microscopy (TEM) using a JEOL JEM-2200FS operating at 200 kV by means of conventional TEM in combination with selected area diffraction (SAED) and scanning transmission microscopy (STEM) with energy-dispersive X-ray spectroscopy (EDS). The TEM lamella was prepared by the lift-out technique using the focused ion beam (FIB) FEI Helios NanoLab 600i. Further investigations were done on this lamella by means of electron backscattered diffraction (EBSD) and transmission Kikuchi diffraction (TKD) employing a JEOL JSM 7800F at 20 kV and 30 kV, respectively, equipped with the EDAX TSL hard- and software.

2.3. First-principles calculations

All DFT-based first-principles calculations in the present work were performed by the Vienna *Ab initio* Simulation Package (VASP) [31] with the ion-electron interaction described by the projector augmented wave (PAW) method [32], the exchange-correction functional described by the generalized gradient approximation (GGA) [33]; and the core configurations of Al and Mo recommended by VASP. After structure relaxations using the Methfessel−Paxton [34] technique, a plane-wave cutoff energy of 520 eV was employed to get accurate total energy in terms of a tetrahedron method incorporating Blöchl correction [35]. In addition, the self-consistency of total energy was converged to at least 10^{-6} eV/atom and the *k*-point mesh employed for each Al_3Mo structure is shown in Sec. 3.4. To estimate equilibrium properties for each structure including equilibrium energy, bulk modulus, and the pressure derivative of bulk modulus, a four-parameter Birch-Murnaghan equation of state (EOS) [36] was employed; see details in Refs. [36,37]. Ancillary calculations of single crystal elastic constants for these Al_3Mo compounds were also performed via an efficient strain-stress approach using the non-zero strains of ±0.007, ±0.01, and ±0.013; see details in Refs. [38,39].

3. Results

In section 3.1 special tools are derived which are employed to evaluate the crystal structure data determined by experimental methods in section 3.2.1 and obtained by theoretical methods in section 3.4. Microstructure analysis on different states are described in section 3.2.2 and 3.3.

3.1. Assessing distortions in fcc superstructures

Let's assume a fcc unit cell spanned by the basis vectors $\mathbf{a}_{0fcc} = a_{0fcc}\mathbf{e}_1$, $\mathbf{b}_{0fcc} = a_{0fcc}\mathbf{e}_2$, $\mathbf{c}_{0fcc} = a_{0fcc}\mathbf{e}_3$, where the orthonormal vectors $\mathbf{e}_1$, $\mathbf{e}_2$ and $\mathbf{e}_3$ span a (Cartesian) reference coordinate system for reference, and where a_{0fcc} is the corresponding cubic lattice parameter. Compiling these three basis vectors in a line vector, one obtains a 3 × 3 matrix containing the components of the basis vectors in column vectors:

$$(\mathbf{a}_{0fcc} \quad \mathbf{b}_{0fcc} \quad \mathbf{c}_{0fcc}) = \begin{pmatrix} a_{0fcc} & 0 & 0 \\ 0 & a_{0fcc} & 0 \\ 0 & 0 & a_{0fcc} \end{pmatrix} \tag{1}$$

Applying some pure (symmetric) strain $\boldsymbol{\varepsilon}$ on $(\mathbf{a}_{0fcc} \quad \mathbf{b}_{0fcc} \quad \mathbf{c}_{0fcc})$ resulting into basis vectors of the strained unit cell spanned by new basis vectors $\mathbf{a}_{fcc}$, $\mathbf{b}_{fcc}$, $\mathbf{c}_{fcc}$:

$$(\mathbf{a}_{fcc} \quad \mathbf{b}_{fcc} \quad \mathbf{c}_{fcc}) = (\mathbf{I}+\boldsymbol{\varepsilon})(\mathbf{a}_{0fcc} \quad \mathbf{b}_{0fcc} \quad \mathbf{c}_{0fcc}). \tag{2a}$$

Thereby, $\mathbf{I}$ is the unit matrix, and the whole of $\mathbf{I}+\boldsymbol{\varepsilon}$ is often described as stretch tensor or Bain distortion, often denoted as $\mathbf{U}$ or $\mathbf{B}$, in particular, in the context of martensite formation [40]. Demanding $\boldsymbol{\varepsilon}$ to be symmetric requires a specific orientation of the deformed basis vectors relative to the original ones. Note that the matrices of the form $(\mathbf{a} \quad \mathbf{b} \quad \mathbf{c})$ etc. correspond to the matrix $(\mathbf{M}^{-1})^T$ introduced mainly as $\mathbf{M}$ in Ref. [41]. That matrix was used by one of the present authors mainly in the form $\mathbf{M}^{-1}$ [42,43].

In case of superstructure formation where the basis vectors of the superstructure (indicated by S) are related with the original basis (lack of primes) by a transformation matrix $\mathbf{A}$ multiplied in the present version as its transpose version to the three-column matrices from Eq. (1) from the right:

$$(\mathbf{a}_S \quad \mathbf{b}_S \quad \mathbf{c}_S) = (\mathbf{a}_{fcc} \quad \mathbf{b}_{fcc} \quad \mathbf{c}_{fcc})\mathbf{A}^T$$

and

$$(\mathbf{a}_{0S} \quad \mathbf{b}_{0S} \quad \mathbf{c}_{0S}) = (\mathbf{a}_{0fcc} \quad \mathbf{b}_{0fcc} \quad \mathbf{c}_{0fcc})\mathbf{A}^T \tag{3}$$

Multiplication of Eq. (2a) by $\mathbf{A}^T$ on both sides yields

$$(\mathbf{a}_{fcc} \quad \mathbf{b}_{fcc} \quad \mathbf{c}_{fcc})\mathbf{A}^T = (\mathbf{I}+\boldsymbol{\varepsilon})(\mathbf{a}_{0fcc} \quad \mathbf{b}_{0fcc} \quad \mathbf{c}_{0fcc})\mathbf{A}^T,$$

which can be transformed by substituting the right sides of Eq. (3) for the left sides to:

$$(\mathbf{a}_S \quad \mathbf{b}_S \quad \mathbf{c}_S) = (\mathbf{I}+\boldsymbol{\varepsilon})(\mathbf{a}_{0S} \quad \mathbf{b}_{0S} \quad \mathbf{c}_{0S}). \tag{2b}$$

From comparison of Eq. (2b) with Eq. (2a) it becomes obvious that the same $\mathbf{I}+\boldsymbol{\varepsilon}$ brings about the same deformation of the fcc and of the superstructure, if the latter is defined via Eq. (3) with respect to fcc and thus refers to the same Cartesian frame of reference as used for the fcc structure.

For an experimentally observed crystal structure which can be conceived as a superstructure related via a matrix $\mathbf{A}$ to an fcc structure, the tensor $\boldsymbol{\varepsilon}$ can be determined numerically by fulfilling the experimentally determined lattice metrics contained in $(\mathbf{a}_S \quad \mathbf{b}_S \quad \mathbf{c}_S)$. However, this requires knowledge of a reasonable value for a_{0fcc}. Knowledge of a_{0fcc} can, however, be avoided by defining $\boldsymbol{\varepsilon}$ as the spontaneous strain in the sense of Ref. [44].[5] Thereby, additional to the symmetry of $\boldsymbol{\varepsilon}$ ($\boldsymbol{\varepsilon} = \boldsymbol{\varepsilon}^T$) and to symmetry invariance with respect to the point group symmetry also additional restrictions (e.g. a zero trace, i.e. $\varepsilon_{11} + \varepsilon_{22} + \varepsilon_{33} = 0$) are imposed. In the sense of Ref. [44] the cases discussed here all belong to the species $m\bar{3}mFXXX$, where *XXX* is the point group symbol of the superstructure phase. If it is ensured that the orientation of $(\mathbf{a}_S \quad \mathbf{b}_S \quad \mathbf{c}_S)$ complies with the settings chosen in Ref. [44], the restrictions of $\boldsymbol{\varepsilon}$ can be taken from that work. The thus determined spontaneous strain, referred to specifically as $\boldsymbol{\varepsilon}_{Aizu}$ in the following, determined without reference to a given a_{0fcc}, is an intrinsic measure for the kind and extent of distortion of a

[5] In that work dedicated to (proper) ferroelastics, superstructure formation had not been considered.

superstructure under consideration.

Out of the fcc superstructures discussed in the introduction, crystallographic data of $L1_2$-Al_3Sc, $D0_{22}$-Al_3Ti and Al_3Nb, $D0_{23}$-Al_3Zr, Al_8Mo_3 and *exp*-Al_3Mo from the literature are analyzed with respect to the spontaneous strain ε_{Aizu} (calculated numerically); see Table 2. Table 2 also contains the eigenvalues and eigenvectors of ε_{Aizu}. Additionally, the square root of the Frobenius norm of ε_{Aizu} is listed, which has been introduced in Ref. [44] as (scalar) measure for the spontaneous strain:

$$x_s = \sqrt{\begin{array}{c}(\varepsilon_{Aizu11})^2 + (\varepsilon_{Aizu22})^2 + (\varepsilon_{Aizu33})^2 \\ +2(\varepsilon_{Aizu12})^2 + 2(\varepsilon_{Aizu13})^2 + 2(\varepsilon_{Aizu23})^2\end{array}}. \quad (4)$$

This kind of second invariant of ε_{Aizu} was shown to be closely related with the direction averaged strain (or with the variance of strain determined by direction averaging, $\sqrt{\bar{\varepsilon}^2}$ [45]).

For the tetragonal structures ($D0_{22}$, $D0_{23}$), x_s can be shown to be related to the deviation t of the axial ratio of the fcc unit cell from unity defined as

$$t = c_{fcc}/a_{fcc} - 1 = c_S/(ka_S) - 1, \quad (5a)$$

with $k = 2$ in case of S = $D0_{22}$ and $k = 4$ in case of S = $D0_{23}$ (listed in Table 2, too) yielding from Eq. (4):

$$x_s = \sqrt{6}\ \frac{t}{3+t} \quad (5b)$$

Hence, in the limit of small distortions, the spontaneous strain x_s is proportional to t.

3.2. As-cast alloys with dual-phase $D0_{22}$+$D0_{22}$' microstructure

3.2.1. Powder X-ray diffraction evidence

All the PXRD patterns of the as-cast Al–Mo–Ti alloys listed in Table 1 contain reflections attributable to the $D0_{22}$-Al_3(Ti,Mo) phase. Depending on the alloy, some of the remaining reflections were attributable to other known Al–Mo–Ti phases, but some further reflections remained uninterpreted. Particularly, simple diffraction patterns were obtained from as-cast $Al_{73}Mo_{22}Ti_5$[6] and $Al_{74}Mo_{21}Ti_5$, the evaluation of which is described based on the PXRD data from the former alloy; see Fig. 4. Several of the uninterpreted reflections appear as symmetric pairs around reflections from the $D0_{22}$ phase. This generated the idea that the uninterpreted reflections originate from an orthorhombically distorted variant of the $D0_{22}$ phase, which is called $D0_{22}$' in the following. Indeed, indexing succeeded with $b_{D0_{22}'} < a_{D0_{22}} < a_{D0_{22}'}$ and $c_{D0_{22}'} \cong c_{D0_{22}}$.

Upon setting up structure models for the Rietveld refinements, it had to be taken into account that the crystal structure of the $D0_{22}$ phase with *I*4/*mmm* space group symmetry has three crystallographic distinct atomic sites. In ideal Al_3Ti there is one Ti site (2 atoms per unit cell) and two independent Al sites (2 and 4 atoms per unit cell). As implied by previous works [23,25,54], the homogeneity range of the $D0_{22}$ phase is not restricted to 75 at.% Al in the Al–Mo–Ti system, i.e., it deviates from the *Al$_3$Ti–Al$_3$Mo* line (see Fig. 3) towards lower Al contents so that Ti/Mo atoms have to occupy one or both of the Al sites. With a single type of radiation, however, the determination of the occupancies of several sites with three different types of atoms (Al, Mo, Ti) is essentially an unsolvable problem [55]. The same holds for the *Immm* structure (*translationengleiche* subgroup of order 2 of the space group *I*4/*mmm* of $D0_{22}$ [50]) of $D0_{22}$' (see Fig. 1, far right). Hence, in turn, it is not possible to reliably determine the composition of $D0_{22}$ and $D0_{22}$' from attempts to refine the occupancies of the atomic sites of the respective phases. Even more, also the refined phase fractions will be affected by the inability to assess the true distribution of the atoms on the different sites. As a pragmatic approach, the structure models for both phases used in the Rietveld refinements involves that only the Ti site is allowed to be occupied by Mo, leading in both cases to a formula $Al_3(Ti_{1-\delta}Mo_\delta)$ with separately refined values of δ (see Table 3).

In order to arrive at convincing Rietveld refinements, the pronouncedly *hkl*-dependent line broadening especially with broad *h*00 reflections and narrow *hh*0 reflections in the case of in particular $D0_{22}$ (but also $D0_{22}$') was accounted for (separately for each phase) by anisotropic microstrain broadening according to Refs. [28,30]. Thereby, the squared full-width at half maximum (B_ε^2) of the microstrain along the diffraction vector amounts:

$$B_\varepsilon^2 = Z^B_{1111}x_1^4 + Z^B_{2222}x_2^4 + Z^B_{3333}x_3^4 + 6Z^B_{1122}x_1^2x_2^2 + 6Z^B_{1133}x_1^2x_3^2 + 6Z^B_{2233}x_2^2x_3^2 \quad (6)$$

with x_i being the components of the unit vector parallel to the diffraction vector in the crystal frame of reference along $[100]_{D0_{22},D0_{22}'}$, $[010]_{D0_{22},D0_{22}'}$ and $[001]_{D0_{22},D0_{22}'}$ and with the refined Z^B_{ijkl} parameters containing information about the variances and covariance of the distribution of the strain around the average (corresponding to zero-strain, i.e. the average lattice parameters, here). Eq. (6) contains the description for the orthorhombic $D0_{22}$' structure, whereas for the tetragonal symmetry of the $D0_{22}$ structure $Z^B_{1111} = Z^B_{2222}$, and $Z^B_{1133} = Z^B_{2233}$ hold additionally. The *hkl*-independent pseudo-Voigt shape of the microstrain broadening was determined by the refined value of a shape parameter η weighting the area-normalised Gaussian component with the factor $(1-\eta)$ and the area-normalised Lorentzian component with η.

Refinement required additionally correction for slight preferred orientation accounting for some too strong measured intensity of reflections (*hkl*) close to the (001) plane normal. It was sufficient (and reasonable in view of the microstructure; see below) to refine the same March-Dollase correction parameters for both phases [51].

The final fitted profile for the $Al_{73}Mo_{22}Ti_5$ is shown in comparison with the experimental profile and the difference curve in Fig. 4. The correspondingly refined parameters have been listed in Table 3. The lattice parameters of $D0_{22}$ and $D0_{22}$' have additionally been included in Table 2 for calculation of the spontaneous strain ε_{Aizu}.

The lattice parameters and phase fractions from PXRD analysis of all the $D0_{22}$' containing as-cast alloys have been included in Table 1. $Al_{74}Mo_{21}Ti_5$, featuring a higher Al content than $Al_{73}Mo_{22}Ti_5$, gave a quite similar diffraction pattern as shown in Fig. 4, interpretable in terms of sole presence of $D0_{22}$ + $D0_{22}$' with a smaller difference $a_{D0_{22}'} - b_{D0_{22}'}$ than observed for $Al_{73}Mo_{22}Ti_5$. $Al_{70}Mo_{24}Ti_6$ is located in a compositional region (see Fig. 3) implying primary solidification of the cubic $Al_{63}(Mo,Ti)_{37}$ phase (occasionally referred to as τ), which rapidly decomposes into Al_8Mo_3, $D0_{22}$, and/or bcc solid solution. The latter phases coexist with $D0_{22}$ + $D0_{22}$' according to the PXRD analysis in $Al_{70}Mo_{24}Ti_6$.

3.2.2. Microstructure evidence

Polished cross sections from as-cast $Al_{73}Mo_{22}Ti_5$ alloy were studied by SEM analysis using BSE contrast, see Fig. 5a. Evidently, within large dendritic grains having grown during solidification a substructure is revealed by contrast differences, which changes along linear directions, being constant within apparently single-

[6] In an earlier work [23] the as-cast microstructure of $Al_{73}Mo_{22}Ti_5$ was claimed to contain Al_8Mo_3. This was caused by a misinterpretation of the SEM microstructure based on local composition measurements.

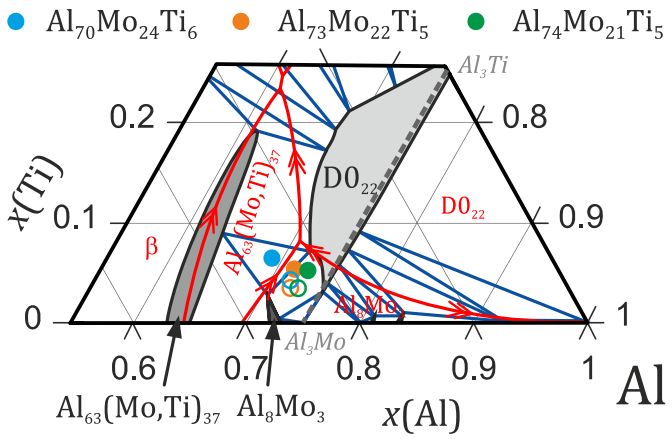

Fig. 3. Al-rich part of the Gibbs composition triangle (in molar fractions x) of the Al–Mo–Ti system indicating the liquidus (red lines separating the primary solidification fields) and solidus projections (grey single-phase fields and blue three-phase triangles) of that system according to Refs. [23,25,26]. The EPMA-based compositions of the as-cast alloys from Table 1 labelled in the text by their nominal compositions is indicated by filled circles whereas open circles indicate EPMA-based compositions of the $D0_{22}$+$D0_{22}$' regions in these alloys. (For interpretation of the references to color in this figure legend, the reader is referred to the Web version of this article.)

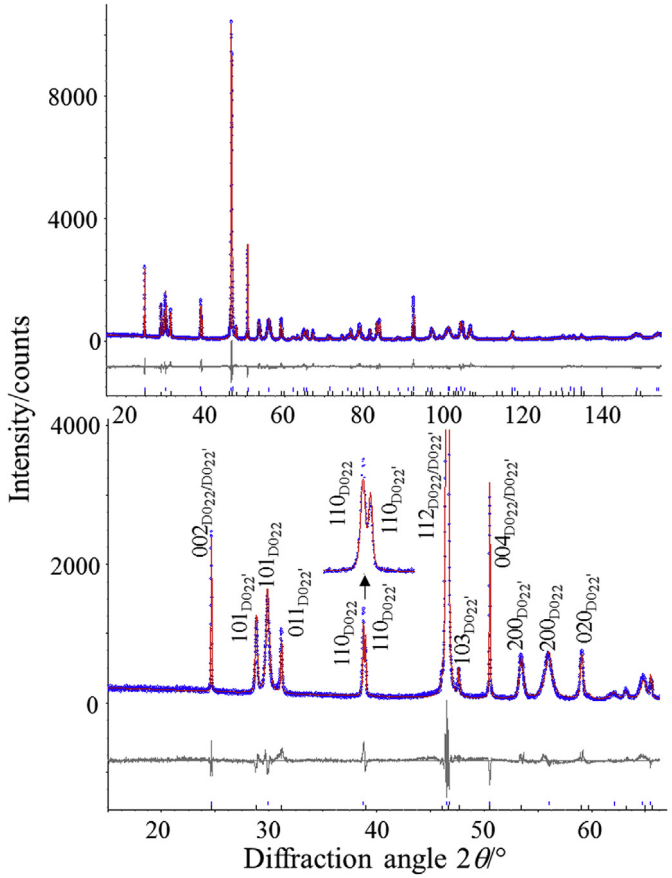

Fig. 4. Powder-X-ray diffraction data from pulverized as-cast $Al_{73}Mo_{22}Ti_5$ alloy recorded with $CoK_{\alpha 1}$ radiation: (top) overview, (bottom) zoomed-in low-angle region with further zoomed $110_{D022}/110_{D022'}$ reflection (inset): Observed data points as well as fitted profile and difference curve from Rietveld refinement (results, see Table 3). Reflect ion markers refer to calculated reflection positions for the $D0_{22}$ (top) and $D0_{22}$' phases (bottom), where prominent reflections are additional marked by their *hkl* indices. Their *l* values divided by 2 yield the indices pertaining to the fcc substructure underlying both crystal structures.

crystalline regions. Hence, the internal structure is most likely dictated by the crystallographic directions of the crystalline phase present in these regions. In view of the quite similar phase fractions of $D0_{22}$ and $D0_{22}$' according to PXRD analysis (see section 3.2.1, Fig. 4, Tables 1 and 3), the substructured regions consist of a mixture of $D0_{22}$ + $D0_{22}$'.

In the lower-Al content alloy $Al_{70}Mo_{24}Ti_6$, SEM in BSE contrast (see Fig. 5b) reveals the presence of primary $Al_{63}(Mo,Ti)_{37}$ dendrites, which are partly or fully decomposed into Al_8Mo_3, $AlMo_3$ and/or bcc during cooling. The interdendritic space is filled with similarly structured material consisting of $D0_{22}$ + $D0_{22}$' as encountered for Fig. 5a.

Preliminary EBSD measurements on the substructured microstructure using the structure models of $D0_{22}$ and $D0_{22}$' revealed mutual occurrence of these phases on a very fine scale with parallel directions $\langle 001\rangle_{D0_{22}}$ and $\langle 001\rangle_{D0_{22}'}$. Since the microstructure was too fine for regular EBSD mapping in reflection geometry, for further microstructure study of the as-cast $Al_{73}Mo_{22}Ti_5$ alloy, a TEM lamella perpendicular to the tentatively identified $\langle 001\rangle_{D0_{22},D0_{22}'}$ direction was extracted by means of FIB milling.

(S)TEM and SAED on this lamella confirmed mutual presence of $D0_{22}$ and $D0_{22}$' in the specimen with parallel $\langle 001\rangle_{D0_{22}}$ and $\langle 001\rangle_{D0_{22}'}$ axes, see Figs. 6 and 7. In Fig. 6 a STEM image showing some pattern of domains is depicted. An EDS scan was performed over the region of this image. The data were only suitable for qualitative interpretation, but clearly show a variation of the intensity of the Mo signal coinciding with the light-dark contrast visible in Fig. 6. By means of SAED (see Fig. 7) the Mo-poorer regions were identified as tetragonal $D0_{22}$, showing, however pronounced streaking into $\{110\}_{D0_{22}}$. More and sharper reflections are encountered in the Mo-richer regions. Within these reflections a significant number are compatible with the $D0_{22}$' structure derived from PXRD (see section 3.2.1). Other surplus reflections could not be attributed to the known superstructures like Al_8Mo_3 or *exp*-Al_3Mo, nor was it yet possible to arrive at a conclusive indexing. It is believed that ordering responsible for these reflections has been introduced by some excitation during TEM specimen preparation.[7]

The TEM specimen was also used for TKD for local phase assignment. The phase separation was mainly relying on the modified angles between the Kikuchi bands for the $D0_{22}$ and $D0_{22}$' phase, in spite of the similarity between the simulated patterns. Due to the wedge shaped character of the TEM-lamella, a uniform background correction was not feasible, therefore, higher number of non-indexed points can be observed in the very thin and the very thick part of the lamella. A predominantly indexed map is shown in Fig. 8, confirming the results from TEM investigations and putting the insight into some statistically more significant basis. Apart from the aforesaid facts, the microstructure shows the following features:

(i) Whereas the directions $\langle 001\rangle_{D0_{22}}$ and $\langle 001\rangle_{D0_{22}'}$ are precisely parallel, $\langle 100\rangle_{D0_{22}}$ and $\langle 100\rangle_{D0_{22}'}$ as well as $\langle 01\rangle 0_{D0_{22}'}$ are only approximately parallel. In fact, it appears, that the $D0_{22}$ phase features two distinct orientations differing by about 6.5° by rotation around $\langle 001\rangle_{D0_{22},D0_{22}'}$ between two $D0_{22}$ regions sharing a common corner. That disorientation angle was

[7] This belief is backed by the observation of well visible Kikuchi bands in the TKD patterns recorded during the TKD investigations described in the remainder section 3.2.2. The corresponding bands were, however, invisible in Kikuchi patterns recorded on conventional cross sectional specimens used e.g. to record the SEM images (see Fig. 5), which is well compatible with non-observation of corresponding reflections in the PXRD data. The reflections encountered in Fig. 7 could correspond to some early stage of the ordering, the detailed study of which is, however, beyond the scope of the present work.

Table 3
Results of the Rietveld refinements on the basis of the PXRD data from as-cast $Al_{73}Mo_{22}Ti_5$ alloy; see Table 1.

Residual values: $R_p = 9.5$, $R_{wp} = 12.4\%$					
Common atomic displacement parameter for all atoms of both phases: $B = 0.011(15)$ Å^2					
March-Dollase preferred orientation parameter as implemented in TOPAS: 001 texture direction: 1.202(2) for both phases					
Site	Wyckoff symbol	x	y	z	Occupation
$D0_{22}$, *I*4/*mmm*, $a_{D0_{22}} = 3.81127(5)$ Å, $c_{D0_{22}} = 8.38221(14)$ Å[a]					
$Z^B_{1111} = 149(12) \times 10^{-6}$, $Z^B_{3333} = 1.8(2) \times 10^{-6}$, $Z^B_{1122} = -43(4) \times 10^{-6}$, $Z^B_{1133} = 0.4(1) \times 10^{-6}$, $\eta = 0.997(4)$					
M	2*a*	0	0	0	0.645(5) Mo remainder Ti[b]
Al	2*b*	0	0	½	1
Al	4*d*	0	½	¼	1
$D0_{22}$', *Immm*, $a_{D0_{22}'} = 3.97762(9)$ Å, $b_{D0_{22}'} = 3.62953(7)$ Å, $c_{D0_{22}'} = 8.38492(13)$ Å[a]					
$Z^B_{1111} = 56.8(10) \times 10^{-6}$, $Z^B_{2222} = 19.7(4) \times 10^{-6}$, $Z^B_{3333} = 0.48(6) \times 10^{-6}$, $Z^B_{1122} = -7.5(2) \times 10^{-6}$, $Z^B_{1133} = 1.5(2) \times 10^{-6}$, $Z^B_{2233} = 2.2(2) \times 10^{-6}$, $\eta = 0.564(13)$					
M	2*a*	0	0	0	0.474(5) Mo remainder Ti[b]
Al1	2*c*	½	½	0	1
Al2	4*j*	½	0	0.2640(3)	1

[a] Lattice parameter considered in Table 2 to calculate strains.
[b] These refined occupancies of Mo and Ti on the 2*a* sites imply compositions of $D0_{22}$-$Al_3(Ti_{0.355}Mo_{0.645})$ and $D0_{22}$'-$Al_3(Ti_{0.526}Mo_{0.474})$. As, however, discussed in the text, these have to be treated with caution as pointed out in section 3.2.1 and 4.2 and unlikely represent reality.

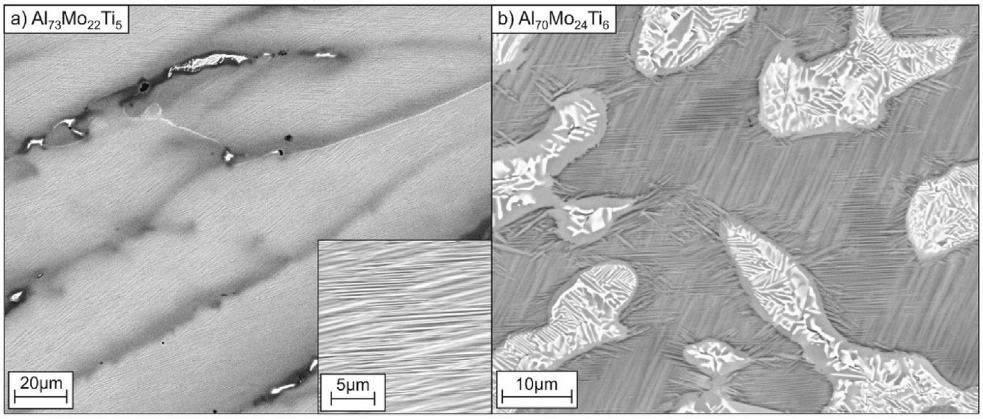

Fig. 5. Scanning electron microscopy images using backscattered electron contrast depicting the microstructure of as-cast (a) $Al_{73}Mo_{22}Ti_5$ alloy (b) $Al_{70}Mo_{24}Ti_6$ from polished, cross-sectional specimens.

determined as an average by determining a couple of disorientation values as indicated by the double arrow in the inverse pole figure (IPF) map shown in Fig. 8.

(ii) Boundaries contain the $\langle 001\rangle_{D0_{22},D0_{22}'}$ direction and are *approximately* oriented on $\{110\}_{D0_{22},D0_{22}'}$. Such boundaries are only observed between $D0_{22}$ and $D0_{22}$', whereas similar boundaries between different orientations of $D0_{22}$' do not occur. The phase boundaries meet in quadruple lines running along $\langle 001\rangle_{D0_{22},D0_{22}'}$. Hence, the boundaries should be classified as phase boundaries. Contrast variations exist also *within* the $D0_{22}$ regions, which are also located on $\{110\}_{D0_{22}}$ planes.

This description emphasizes the appearance of the microstructure when viewed as a cross section perpendicular to $\langle 001\rangle_{D0_{22},D0_{22}'}$. Along the $\langle 001\rangle_{D0_{22},D0_{22}'}$ directions, however, the grains appear to have, by far, the longest extension. That one-dimensional character is obviously origin of the stripy contrast of randomly cut grains crystalline regions visible in the SEM images (see Fig. 5).

3.3. Dual phase microstructures $D0_{22}$ + Al_8Mo_3 in annealed $Al_{73}Mo_{22}Ti_5$

A piece of the as-cast $Al_{73}Mo_{22}Ti_5$ alloy was annealed for 12 h at 1400 °C. PXRD data (not shown; results summarized in Table 1) reveal the presence of $D0_{22}$ + Al_8Mo_3, whereby the reflections of $D0_{22}$ still shows the pronounced anisotropic line broadening. Also tiny reflections attributable to remainders of $D0_{22}$' are visible.

SEM investigations in BSE contrast reveal presence of granular precipitates of lighter contrast embedded in a darker matrix. Fig. 9 shows the results of EBSD mappings for such a region with precipitates indexed with tetragonal $D0_{22}$ and monoclinic Al_8Mo_3. While, according to the IPF map, the $D0_{22}$ phase shows largely uniform orientation with some scatter around the $\langle 001\rangle_{D0_{22}}$ direction, the Al_8Mo_3 precipitates appear to adopt four distinct orientations with respect to the surrounding $D0_{22}$ phase. These four orientations can be rationalized by comparing the orientations $\langle 100\rangle_{fcc}$ corresponding to $\langle 100\rangle_{D0_{22}}$ and $\langle 001\rangle_{D0_{22}}$ as well as to $\langle \bar{1}04\rangle_{Al_8Mo_3}$, $010_{Al_8Mo_3}$ and $502_{Al_8Mo_3}$ directions. The indicated directions of Al_8Mo_3 are those which correspond to the $\langle 100\rangle_{D0_{22}}$ and $\langle 001\rangle_{D0_{22}}$ directions (or simply $\langle 100\rangle_{fcc}$[8]) in view of the **A** matrices listed in Table 2. While all four directions of Al_8Mo_3 have the

[8] This can be rationalized by using the $\mathbf{A}^T$ matrices listed in Table 2 relating the unit cells of the superstructure (superst.) via $\begin{pmatrix} u \\ v \\ w \end{pmatrix}_S = \mathbf{A}^{-T} \begin{pmatrix} u \\ v \\ w \end{pmatrix}_{fcc}$, where −T correspond to inverse-transpose of **A**.

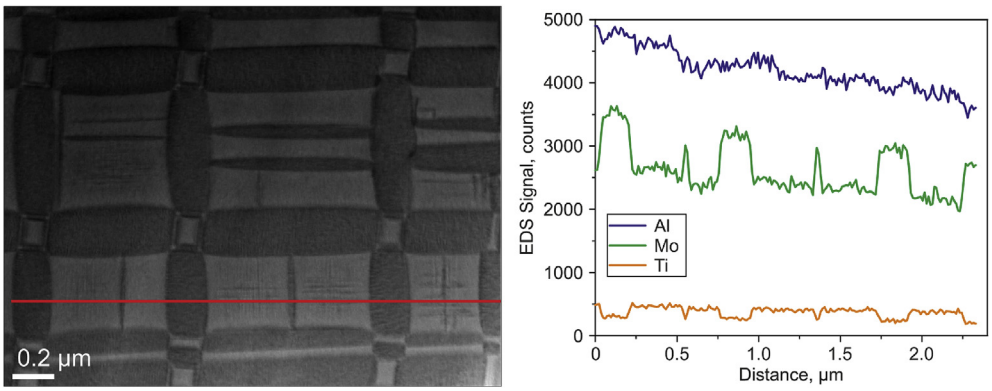

Fig. 6. (left) STEM micrograph of a thin lamella of as-cast $Al_{73}Mo_{22}Ti_5$ alloy with $[001]_{D0_{22},D0_{22}'}$ incidence direction revealing a nanoscopic domain microstructure. (right) EDS line scan (red horizontal line on the left) revealing qualitative values for the Mo contents being higher in the dark-contrast domains ($D0_{22}$'; see Fig. 7) and lower in the bright-contrast domains ($D0_{22}$; see Fig. 7). (For interpretation of the references to color in this figure legend, the reader is referred to the Web version of this article.)

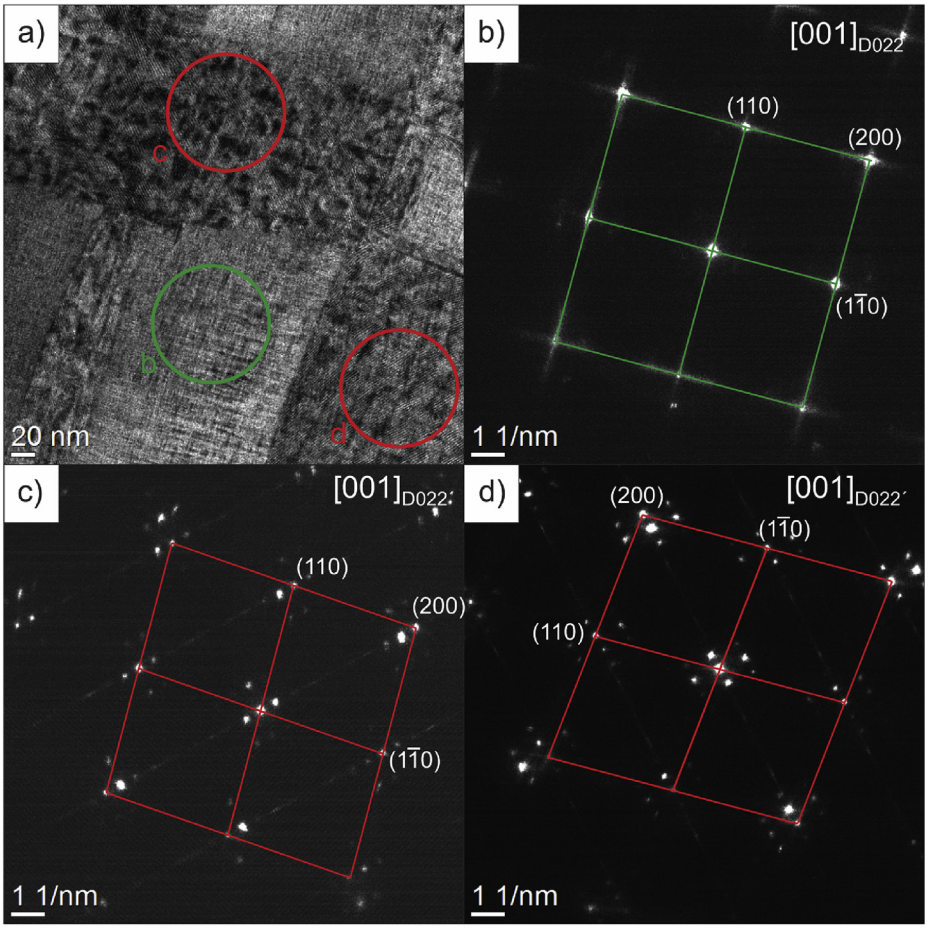

Fig. 7. (a) TEM bright-field micrograph of a thin lamella of as-cast $Al_{73}Mo_{22}Ti_5$ alloy with $[001]_{D0_{22},D0_{22}'}$ (same as is Fig. 6). The circles labelled with (b–d), illustrate the irradiated areas of the respective SAED diffraction patterns shown in (b–d) (b: $D0_{22}$, (c, d): $D0_{22}$'. The *hkl* indices refer to the respective unit cell (compare Table 3). Note that additional reflection in (c, d) are due to double diffraction or due to some superstructure (which likely has developed during sample preparation; not identical with Al_8Mo_3, see text).

direction $\langle 502\rangle_{Al_8Mo_3}$ in common, which is parallel to $\langle 001\rangle_{D0_{22}}$ of the $D0_{22}$ matrix, the directions $\langle \bar{1}04\rangle_{Al_8Mo_3}$ and $\langle 010\rangle_{Al_8Mo_3}$ are parallel to $\langle 100\rangle_{D0_{22}}$, leading to the four different orientation variants which differ by rotations of 90° around $\langle 502\rangle_{Al_8Mo_3}$ / $\langle 001\rangle_{D0_{22}}$.

3.4. First-principles calculations

First-principles calculations have been performed from a couple of structures having, for simplicity all the composition Al_3Mo, as listed in Table 4.[9] These structures involve (i) the experimentally encountered *exp*-Al_3Mo structure [21]; (ii) an *alternative* version of the Al_3Mo structure (*alt*-Al_3Mo) derived to contain only the pairs of

[9] *exp*-Al_3Mo is much less frequently observed experimentally as compared to Al_8Mo_3, because the latter phase has a very high congruent melting temperature of about 1560 °C, involving an extended primary solidification field (see Fig. 3), whereas *exp*-Al_3Mo only forms by a peritectoid reaction at about 1220 °C [21].

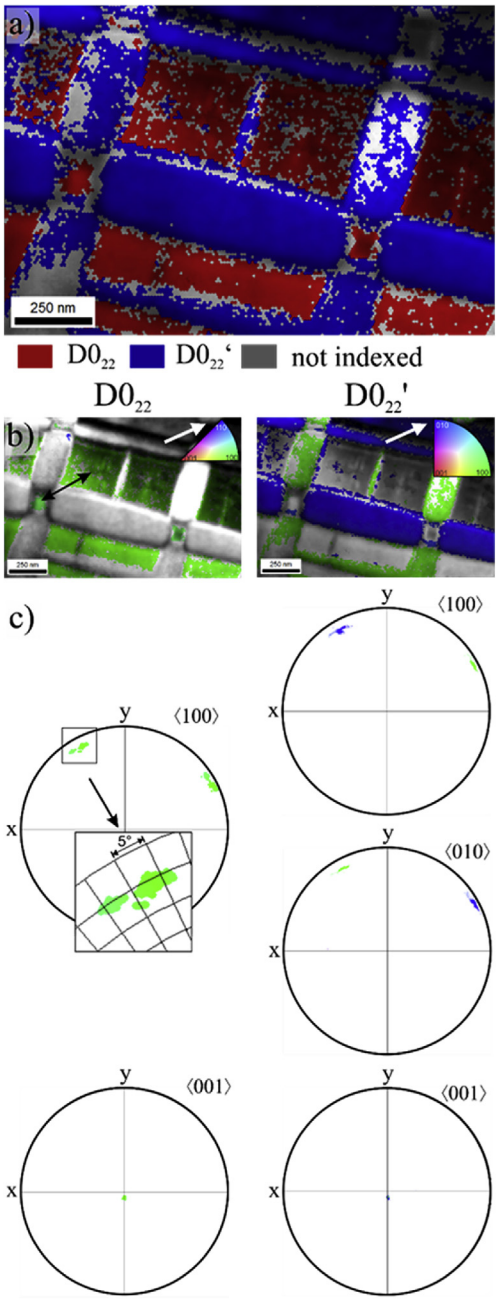

Fig. 8. Transmission Kikuchi diffraction analysis from the TEM specimen used in Fig. 7: (top) phase map with phase specific colors, (middle) phase specific IPF maps with color referring to the white arrow within the TEM foil chosen to enhance the color contrast as well as (bottom) corresponding pole figures with indicated directions. The $D0_{22}$' variants differ by a 90° rotation around $\langle 001\rangle_{D0_{22}.D0_{22}'}$. The different $D0_{22}$ variants (black double arrow in IPF map) exhibit orientations differing by ~6.5° around $\langle 001\rangle_{D0_{22}.D0_{22}'}$ from each other as also visible from the pole figure (magnification). (For interpretation of the references to color in this figure legend, the reader is referred to the Web version of this article.)

Mo atoms already contained in *exp*-Al_3Mo (see Fig. 2, respectively); (iii) $D0_{22}$-Al_3Mo, and (iv) $L1_2$-Al_3Mo (see Fig. 1, respectively). Structure relaxations under symmetry restriction of the space groups indicated in Table 4 give lattice parameters which have been included in Table 2. Application of the procedure to determine equilibrium properties by Birch-Murnaghan EOS [36] fittings gives the results listed in Table 4, including the bulk modulus B and the pressure derivative of bulk modulus B'.

Exploration of the energy space around the relaxed structures revealed elastic instability for the $D0_{22}$ and the $L1_2$ structures. Off-symmetric, elastically stable energy minima were formed upon orthorhombic and tetragonal distortion, yielding data included as $D0_{22}$' and $L1_2$' in Tables 2 and 4

The final structure parameters of *exp*-Al_3Mo conform with $C2/m$ symmetry (see also footnote to Table 2), a symmetry, which is also closely fulfilled by the reported results of the experimental structure refinement [21] and the drawing in Fig. 2. The lattice parameters also agree reasonably well with experimentally obtained data, especially when it comes to the shape of the unit cell; see also section 4.1. This *exp*-Al_3Mo crystal structure was also the lowest-energy one of those considered here, conforming with experimental evidence (thereby ignoring $T \neq 0$ K effects on structural stability).

Among the initially explored high-symmetry structures, hypothetical tetragonal $D0_{22}$-Al_3Mo showed the second-lowest energy which is by 61 meV/atom larger than for *exp*-Al_3Mo. This $D0_{22}$-Al_3Mo, however, exhibits a negative shear modulus $\frac{1}{2}(C_{11} - C_{12}) = (157-176)/2$ GPa with C_{ij} being the corresponding components of the Voigt-type 6×6 matrix representation of the elastic stiffness in standard orientation for tetragonal symmetry. Strain relaxation then ends up in elastically stable orthorhombic $D0_{22}'$-Al_3Mo in *Immm* symmetry, having an energy of 59 meV/atom higher than the *exp*-Al_3Mo. Higher energies are obtained for *alt*-Al_3Mo and, in particular, for $L1_2$/$L1_2$'.

4. Discussion

Section 4.1 puts together evidence from the literature and theoretical information obtained in section 3.4 to derive common and differing structural characteristics of the stable fcc-based superstructure phases under consideration. This prepares for discussing the experimental evidence from section 3.2.1 on the structural characteristics of the newly discovered $D0_{22}$' phase in section 4.2. Section 4.3 discusses the microstructures $D0_{22} + D0_{22}$' as well as $D0_{22} + Al_8Mo_3$ characterized in sections 3.2.2 and 3.3 in view of the structural characteristics of these phases. In all sections the tools derived for structure analysis in section 3.1 are employed.

4.1. Character of the fcc-based equilibrium superstructure phases

The spontaneous strain ε_{Aizu} exhibited by the considered, experimentally known *TM* aluminides with fcc superstructure (trialuminides in $L1_2$, $D0_{23}$, $D0_{22}$ structures, Al_8Mo_3, *exp*-Al_3Mo; see Table 2) can be related, on an empirical basis, to the type of *TM*−Al ordering present in the superstructure as expressed in terms of the frequency *TM*−*TM* pairs. Since, except for Al_8Mo_3 and *exp*-Al_3Mo, only the 2nd-next-neighbor (n.n.) *TM*−*TM* pairs occur, the effect of these types of pairs will be considered first. The fractions of such pairs have been determined by counting the numbers of corresponding pairs in a unit cell and have been compiled, separately for each of the $\mathbf{e}_1$-$\mathbf{e}_3$ directions, in Table 5. Note that these 2nd-n.n. pairs point along the $\langle 100\rangle_{fcc}$ directions, whereas the 1st-n.n. pairs point along $\langle 110\rangle_{fcc}$ (see Figs. 1 and 2).

Within the series of $L1_2$, $D0_{23}$ and $D0_{22}$ (see Fig. 1) the fraction of 2nd-n.n. *TM*−*TM* pairs along $\mathbf{e}_3$ decreases to zero, whereas the fraction of such pairs along $\mathbf{e}_1$ and $\mathbf{e}_2$ remains constant. This is connected with introducing the antiphase boundaries with respect to $L1_2$ indicated in Fig. 1. Inspecting the spontaneous strains compiled in Table 2, the encountered increase of "tetragonality" with $1 + t = c_{fcc}/a_{fcc} > 1$ upon leaving the cubic $L1_2$ structure towards $D0_{23}$ and $D0_{22}$, implies (sorted) eigenvalues of the type $-s$, $-s$, $+2s$ (s positive), with the eigenvector pertaining to the

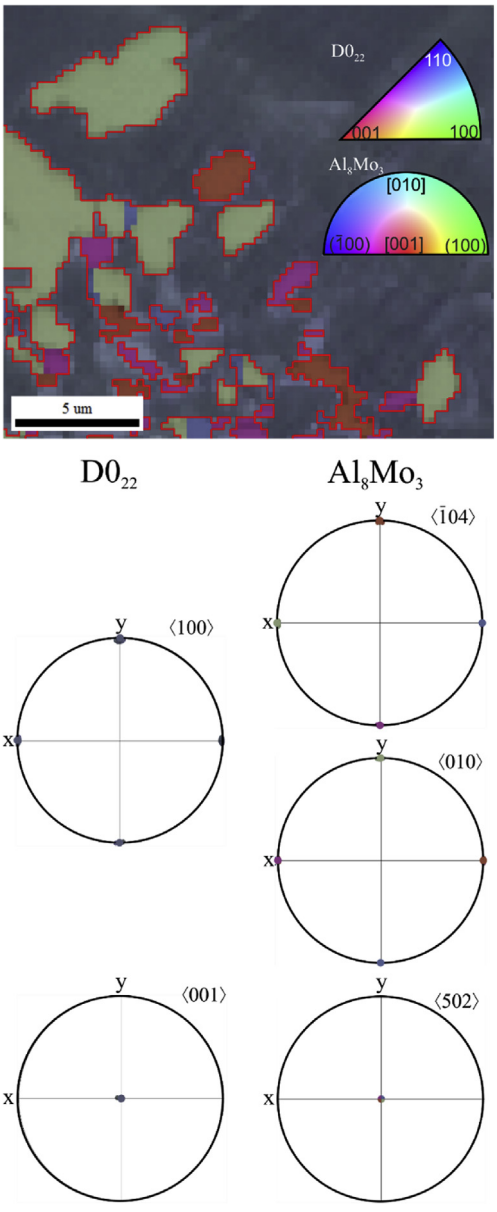

Fig. 9. Cross-sectional electron backscatter diffraction analysis of $Al_{73}Mo_{22}Ti_5$ annealed for 12 h at 1400 °C: (top) inverse pole figure map displaying the orientation of the $D0_{22}$ matrix (dark blue with largely uniform orientation) and Al_8Mo_3 precipitates of different orientations, and (bottom) pole figures pertaining to different directions of the phases corresponding to $\langle 100\rangle_{fcc}$ directions in both phases. Note that the sample coordinate system was adjusted to yield a simple orientation for the $D0_{22}$ phase. The four different variants of the Al_8Mo_3 phase share a common $\langle 502\rangle_{Al_8Mo_3}$ axis parallel to $\langle 001\rangle_{D0_{22}}$, whereas the $\langle \bar{1}04\rangle_{Al_8Mo_3}$ and $\langle 010\rangle_{Al_8Mo_3}$ directions point parallel to $\langle 100\rangle_{D0_{22}}$. (For interpretation of the references to color in this figure legend, the reader is referred to the Web version of this article.)

last (largest) eigenvalue being parallel to $\mathbf{e}_3$ (indicated by red arrows in Fig. 1; perpendicular eigenvectors in green pertaining to $-s$). Notably, the smaller distortion (smaller s) of the $D0_{23}$ example than for the examples given for $D0_{22}$ in Table 2, a trend also reflected by lattice parameters obtained from relaxed DFT calculations on $D0_{22}$-and $D0_{23}$-Al_3Ti [9]. This difference can be related to the intermediate fraction of 2nd-n.n. *TM*−*TM* pairs in $D0_{23}$ as compared to $L1_2$ and $D0_{22}$. Hence, presence of 2nd-n.n. *TM*-*TM* pairs along a crystallographic direction appears to increase the lattice distances in their direction. In $L1_2$, the effect for the directions parallel to $\mathbf{e}_1$-$\mathbf{e}_3$ is balanced, and the structure is cubic, whereas the effect comes into play for $D0_{23}$ and even more in $D0_{22}$ in the form of the tetragonal metric as expressed in terms of s or t.

In Al_8Mo_3 and *exp*-Al_3Mo, the long-range order of the *TM* atoms changes further with respect to $D0_{22}$ (i.e., upon going from group-v to group vi *TM*) although some features, and even fragments of the $D0_{22}$ structure (see rectangles in Fig. 2) remain present. As indicated in Table 5, upon going from $D0_{22}$ to Al_8Mo_3 and *exp*-Al_3Mo, the absence of 2nd-n.n. *TM*−*TM* pairs along $\mathbf{e}_3$ is retained,[10] as it is also the case for retention of the maximum possible fraction of such pairs along $\mathbf{e}_2$. The number of such pairs along $\mathbf{e}_1$ is, however, reduced to values intermediate between those of $\mathbf{e}_2$ and $\mathbf{e}_3$, at the cost of formation of 1st-n.n. *TM*-*TM* pairs along the direction $\mathbf{e}_1$+$\mathbf{e}_3$. This appears to be reflected by eigenvalues approximately like $-s$, 0, s (see Table 2). In both Al_8Mo_3 and *exp*-Al_3Mo, the eigenvector pertaining to the smallest eigenvalue ($\approx -s$) points along $\mathbf{e}_2$ (blue arrows in Fig. 2), the direction with the largest fraction of 2nd-n.n. *TM*−*TM* pairs. The other eigenvectors pertaining to the intermediate (≈ 0, blue) and largest ($\approx +s$, red) eigenvalues point more or less (*exp*-Al_3Mo) approximately along $\mathbf{e}_1$ and $\mathbf{e}_3$, corresponding with the intermediate and lowest fraction of 2nd-n.n. *TM*−*TM* pairs. Note, that the eigenvectors are, somewhat, tilted away from these directions such that the direction of the eigenvector with the largest eigenvalues (red; see Fig. 2) tends to move into the direction of the 1st-n.n. *TM*−*TM* pairs oriented along $\mathbf{e}_1$+$\mathbf{e}_3$ (there are no the 1st-n.n. pairs along other $\langle 110\rangle_{fcc}$ directions). This is the case for both Al_8Mo_3 and *exp*-Al_3Mo, but also for the hypothetical *alt*-Al_3Mo structure taking into account the structure parameters from first-principles calculations. This indicates, that not only the 2nd-n.n. but also the 1st-n.n. *TM*−*TM* pairs have a characteristic effect on the distortions of the crystal structure due to *TM* ordering.

4.2. $D0_{22}$' in view of equilibrium phases

For further discussion it seems crucial to assess the composition of the $D0_{22}$ and $D0_{22}$' based on the experimental data. As indicated in section 3.1, the evaluations of the PXRD results can, in the present case, not be used to assess the composition. The alloy compositions and, in particular, the local EPMA measurements in the $D0_{22}$ + $D0_{22}$' regions (see Table 1 and Fig. 3) imply Al contents <75 at.% and generally a narrow compositional window somewhat more Mo-rich than the corresponding to the nominal compositions of the two dual-phase alloys $Al_{73}Mo_{22}Ti_5$ and $Al_{74}Mo_{21}Ti_5$. On a local scale, the EDS line scan on the TEM specimen convincingly indicates higher Mo and lower Ti contents in the $D0_{22}$' phase than in the $D0_{22}$ phase (see Fig. 6). Due to the only qualitative reliability of the EDS data, the actual concentration difference between $D0_{22}$ and $D0_{22}$' remains undetermined. In any case, the already high Mo content of $D0_{22}$ + $D0_{22}$' in combination with some concentration difference with a higher Mo content for $D0_{22}$' implies Mo depleted $D0_{22}$, coming closer to the extent of the $D0_{22}$ field in the solidus projection; see Fig. 3. Hence, the composition in $D0_{22}$' should be very close to the binary Al_8Mo_3 and *exp*-Al_3Mo phases. In view of this, it is not surprising the eigenvalues of the spontaneous strain ε_{Aizu} for the experimentally encountered $D0_{22}$' phase show the same approximately sequence $-s$, 0, s as encountered experimentally and by first-principles

[10] Note that the Cartesian coordinate axes have deliberately been chosen upon choosing between different possibilities for the matrix $\mathbf{A}^T$ in Table 2, such that structurally similar $\langle 100\rangle_{fcc}$ direction are associated with the same vector out of $\mathbf{e}_1$, $\mathbf{e}_2$ and $\mathbf{e}_3$. This choice, which could be made after having understood the structural trends.

Table 4
Results of equation-of-state (EOS) fitting based on first-principles calculations (by VASP code) for various candidate structures of composition Al_3Mo. Relaxed crystallographic data have been included into Table 2.

Name	Space group	*k*-mesh used for VASP	Formula units per conventional unit cell	Energy (meV/atom)[a]	*B* (GPa)	*B*′
exp-Al_3Mo	*C*2/*m*	3 × 12 × 5	8	0	134.5	4.3
alt-Al_3Mo	*C*2/*m*	9 × 21 × 10	4	74.5	122.5	4.5
$D0_{22}$	*I*4/*mmm*	17 × 17 × 8	2	60.6[b]	138.5	4.3
$D0_{22}'$	*Immm*	19 × 21 × 9	2	58.8	138.5	4.2
$L1_2$	$Pm\bar{3}m$	20 × 20 × 20	1	224.2[b]	135.0	4.2
$L1_2'$	*P*4/*mmm*	19 × 21 × 10	1	204.8	133.7	4.4

[a] Relative to *exp*-Al_3Mo.
[b] Elastically instable indicated by negative values of $(C_{11} - C_{12})$ as well as large fluctuations of C_{ij} values caused by VASP settings, where the predicted C_{ij} values are not shown herein.

Table 5
Fraction of 2nd-next neighbor *TM*−*TM* pairs among all corresponding atom-atom pairs along the different $\langle 100\rangle_{fcc}$ in terms of the Cartesian $\mathbf{e}_1$-$\mathbf{e}_3$ directions defined as in Figs. 1 and 2 (or Table 2). The difference between the values can be related with the eigenvalues of the Aizu strain tensors typically found for the structure types (see Table 2).

Structure type	$\mathbf{e}_1$	$\mathbf{e}_2$	$\mathbf{e}_3$
$L1_2$	0.250	0.250	0.250
$D0_{23}$	0.250	0.250	0.125
$D0_{22}$	0.250	0.250	0
Al_8Mo_3	0.182	0.273	0
exp-Al_3Mo	0.125	0.250	0
alt-Al_3Mo	0	0.250	0

methods for Al_8Mo_3 and *exp*-Al_3Mo but also by first-principles methods for $D0_{22}$'-Al_3Mo (see Table 2).

The elastic instability predicted theoretically for the tetragonal $D0_{22}$-Al_3Mo (see section 3.4) contrasts with the stability of $D0_{22}$-Al_3Ti [52], implying a phase transition tetragonal $D0_{22}$ → orthorhombic $D0_{22}$' on the *Al*$_3$*Ti*−*Al*$_3$*Mo* line to occur for $D0_{22}$/$D0_{22}$'-Al_3(Ti,Mo) structures: with increasing Mo content the shear modulus $\frac{1}{2}(C_{11}-C_{12})$ decreases, finally becoming negative, bringing about the transition. These two phases occurring on the *Al*$_3$*Ti*−*Al*$_3$*Mo* line differing by composition and the phase transition can be regarded as an idealized version of the experimentally encountered phases in the $D0_{22}$ + $D0_{22}$' microstructure, however, with $x_{Al} < 0.75$. PXRD from that microstructure revealed in particular tetragonal $D0_{22}$ pronounced anisotropic microstrain broadening with $Z^B_{1122} = -1/3\ Z^B_{1111}$, which is typical for materials with corresponding elastic anisotropy (compare microstrain broadening exhibited by tetragonal Pb_3O_4 [53]), and which is straightforwardly reconciled with the idea that microstrain broadening is large in directions of large reciprocal Young's modulus [30].

Beyond all this, the spontaneous orthorhombic distortion predicted by first-principles calculations for $D0_{22}$'-Al_3Mo as well as the encounter of a corresponding (long-range) ordering for the experimentally observed $D0_{22}$' phase demonstrates that such a orthorhombic metric with its characteristic spontaneous strain $\boldsymbol{\varepsilon}_{Aizu}$ actually does not require the symmetry breaking by the unequal numbers of 2nd n.n. *TM*−*TM* pairs (for the latter see Table 5) discussed in section 4.1 as related with the spontaneous strain in particular in *exp*-Al_3Mo, Al_8Mo_3 and *alt*-Al_3Mo. Instead, it is believed that there are electronic origins leading to the elastic instability of $D0_{22}$-Al_3Mo. The *exp*-Al_3Mo structure occurs (and Al_8Mo_3) likely occurs in reality due to some additional ordering further stabilizing the distortion already present for electronic reasons.

From these observations it can be concluded that substitution of Ti by the more electron-rich, group-iv element Mo induces structural changes, which can be regarded as a continuation of the structure series $L1_2$ via $D0_{23}$ to $D0_{22}$ occurring for transition metal trialuminides Al_3TM with increasing number of electrons per atom (see Fig. 1). Both the experimentally encountered $D0_{22}$' (as indicated in Table 1 on the far right) and the experimentally known *exp*-Al_3Mo phase (but also Al_8Mo_3) can regarded as the product of similar structure changes due to the increase of the average number of electrons per atom. That number is $e/at = 11.25$ for the ideal composition Al_3Mo, and $e/at = 11.09$ for Al_8Mo_3, whereas on the basis of the current results no definite electron number per atom can be given for the currently observed $D0_{22}$' due to its unknown composition.

Notably, alloying Al_3Ti with the group-vi element chromium leads to a substitution of Al by Cr leading to formation of a $(Al_{2.68}Cr_{0.32})Ti$ phase with $e/at = 10.19$ [56]. Accordingly, this ternary phase (like other related $(Al,X)_3Ti$ phases with $X = 3d$ metals of group number > vi [2]) adopts the $L1_2$ structure, i.e. starting from Al_3Ti the structure series depicted in Fig. 1 is followed into the direction of lower numbers of electrons per atoms, i.e. opposite direction is followed in case of Mo, which substitutes mainly, but not exclusively Ti.

One may guess that similar structure phenomena like the $D0_{22}$' phase might occur in other Al_3TM related systems, evidently Al−Mo−*X* systems with *X* = V, Nb, Ta, Zr, and Hf. Also analogous systems with W instead of Mo (however, fcc related Al−W phases like Al_3W or Al_8W_3 seem to be unknown), or substitution of Al in group-iv/v Al_3TM by electron-rich Si might lead to alloys containing $D0_{22}$' phases with $e/at > 11.0$. Indeed, a literature search for $D0_{22}$'-related structural phenomena in other systems gave evidence for the Al−Nb−Mo system, where in as-cast alloys a ternary phase with "$TiAl_3$-type unit cell" and split reflections involving a possible monoclinic has been mentioned in the passing [57].

4.3. Discussion of microstructures

The $D0_{22}$ + $D0_{22}$' microstructure observed in the as-cast alloys (see Figs. 5–8) consists of both phases in an approximate cube-on-cube orientation relationship with respect to the fcc substructure. The directions of largest positive Aizu strain (eigenvectors with the largest eigenvalues; see Table 2) corresponding to $\langle 001\rangle_{D0_{22}}$ and $\langle 001\rangle_{D0_{22}'}$ are parallel to each other, suggesting that strain is already minimized in that direction. The microstructure consists mainly of alternate, approximately rectangular grains separated by phase boundaries on approximately $\{110\}_{D0_{22}/D0_{22}'}$, meeting in quadruple lines (and not, as usual in grain structures, in triple lines). Details of such a microstructure can be predicted upon demanding that $D0_{22}$' forms from $D0_{22}$ via an invariant plane strain (IPS), i.e. by applying a deformation gradient **F** to $D0_{22}$ to obtain $D0_{22}$' which achieves continuity between these phases upon deformation. Thereby concepts used in the crystallography of martensitic transformations are used [50,58] (PTMC; Phenomenological theory of Martensite

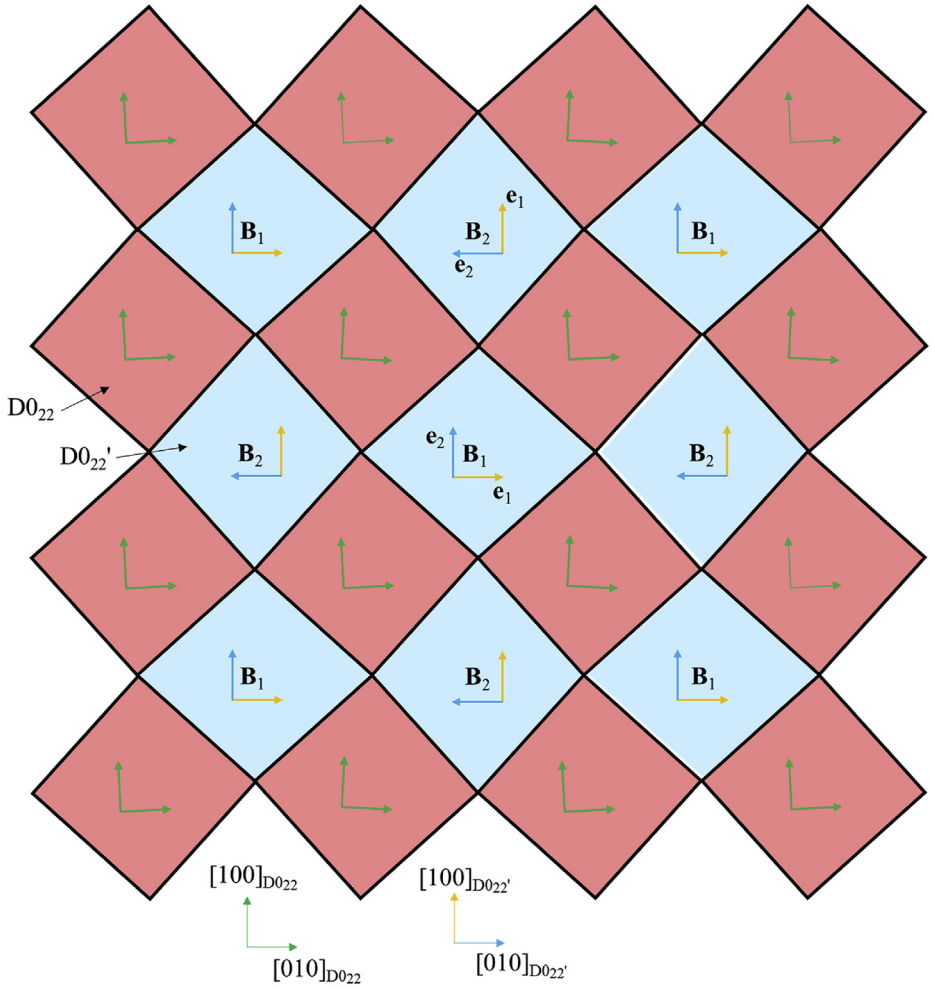

Fig. 10. Sketch of the idealized tetragonal $D0_{22}$ + orthorhombic $D0_{22}$' microstructure in view along $\langle 001\rangle_{D0_{22},D0_{22}'}$. Note the occurrence of two orientations of the $D0_{22}$' phase differing by a rotation of 90° around $\langle 001\rangle_{D0_{22},D0_{22}'}$, as well as the occurrence of two orientations of the $D0_{22}$ phase differing by a rotation of 5.2° around $\langle 001\rangle_{D0_{22},D0_{22}'}$ (experiment 6.5°, compare Fig. 8).

Crystallography), which are known to be applicable, to some extent, to many phase transformations, in which diffusion plays a role, e.g. to accomplish compositional change.

Corresponding considerations detailed in the appendix predict an idealized microstructure depicted in Fig. 10. The checkerboard derived consists of alternate $D0_{22}$ and $D0_{22}$' domains, where the latter have the required alternate $D0_{22}$' orientations. Moreover, alternate $D0_{22}$ grains assume two distinct orientations differing by $2 \times 2.6 = 5.2°$ (as derived from the lattice parameters in the appendix). This value is well compatible with the value of 6.5° derived from the orientation data in Fig. 8. Note that the idealized microstructure consists of squares for $D0_{22}$ and rhombs for $D0_{22}$'. However, the derived IPS conditions can be maintained by having rectangular $D0_{22}$ grains and parallelogram shaped $D0_{22}$', as well as unequal sizes of the $D0_{22}$ regions of the two different orientations encountered experimentally (compare Fig. 8). The habit plane is predicted to be closely to {110} for both $D0_{22}$ and $D0_{22}$'.[11] The obviously non-planar boundary planes encountered experimentally obstruct more a detailed comparison with the habit planes predicted in the appendix. Such non-planar planes are indicative for residual misfit beyond the predicted IPS, but also for some wedge-disclination-like misfit at the unusual quadruple boundary lines. As it can be shown on the basis of the appendix, such misfits need not exist if the transformation occurs under invariant IPS conditions. However, such conditions are too idealized to explain all features of the microstructure for the following reasons:

a) The concentration difference between $D0_{22}$ and $D0_{22}$' regions requires diffusion to occur.
b) Even if at a certain, elevated temperature the microstructure develops under IPS conditions, misfit induced by differences in the thermal expansions of $D0_{22}$ and $D0_{22}$' may induce stresses.

In fact, the "luckily" absent misfit between $c_{D0_{22}}$ and $c_{D0_{22}'}$ (strain of 0.03%) was derived from the PXRD data, suggesting that this technique yields stress-unaffected lattice parameters. The first-principles-based lattice parameters of $D0_{22}$- and $D0_{22}'$-Al_3Mo indicate by an amount of 0.3%, which would be well detectable by PXRD. Such a misfit, however, also might be accommodated elastically so that lattice parameters derived from PXRD would imply a smaller misfit.

Similar checkerboard microstructures like that encountered

[11] The streaking observed in electron diffraction of the $D0_{22}$ grains along {110} directions in reciprocal space (see Fig. 7) might originate from plate-like orthorhombic regions *within* the tetragonal $D0_{22}$ phase with habit planes again corresponding to {110}. Contrasts visible in corresponding bright-field/TEM images seem to support this.

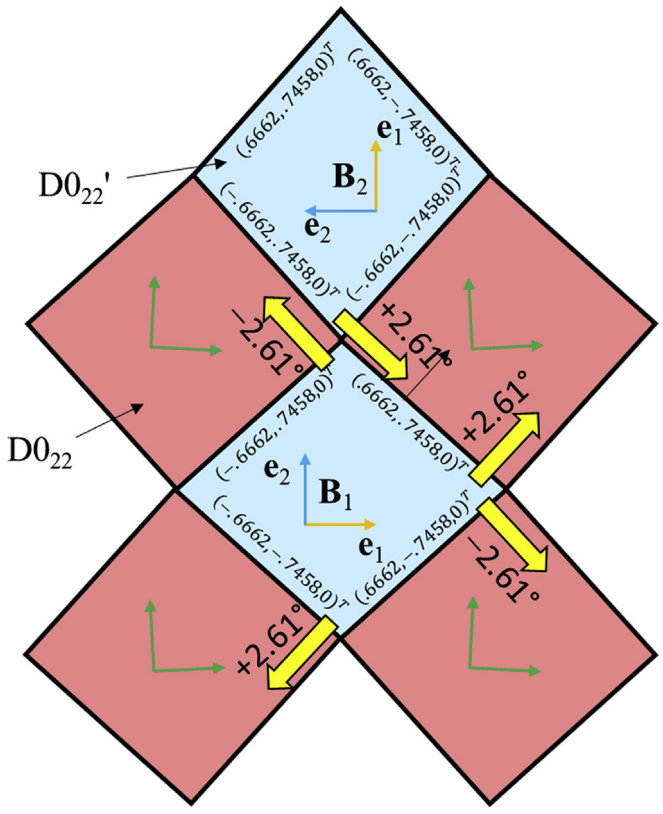

Fig. A1. Part of the idealized D0$_{22}$ + D0$_{22}$' microstructure as derived from an invariant plane strain condition for the interface between the two phases. Two D0$_{22}$' with orientations differing by 90° are depicted with the bounding planes with normal vectors $\{.6662, .7458, 0\}^T$ with respect to the Cartesian coordinate systems shown for the two variants. The thick yellow arrows indicate the rotation of the D0$_{22}$ with respect to D0$_{22}$', resulting in in two distinct orientations of the D0$_{22}$ phase differing by 5.2°.

here for D0$_{22}$+D0$_{22}$' have been reported in a couple of different two-phase systems ([59] and citations therein). Most of the cases mentioned in that work are microstructures from a cubic and tetragonal phase, like the microstructure forming from fcc base L1$_2$+L1$_0$ structured phases in the Co–Pt system upon demixing [60], or L1$_2$ or fcc + D0$_{22}$ in Ni–V–Al based alloys [61,62]. A notable exception is microstructures in Ti-rich Al–Nb–Ti alloys [63], which form D0$_{19}$ + O phase (both hcp based, hexagonal + orthorhombic). Apparently, a tetragonal/orthorhombic case has not been encountered so far.

The formation of the present microstructure might occur in a similar way as in the Co–Pt example [60]. Upon likely non-equilibrium solidification leading in the present case initially to grains of single-phase and single-orientation D0$_{22}$, demixing occurs, e.g. in a spinodal fashion. More research is required to clarify this picture. However, already the results from the further annealing indicate (see section 3.3) the formation of the equilibrium Al$_8$Mo$_3$ phase besides D0$_{22}$. The currently observed microstructure with D0$_{22}$' is, hence, most likely a transitional state during the demixing process of D0$_{22}$ supersaturated with respect to Mo. As shown in section 4.1 the transitional D0$_{22}$' already shows similar distortions as the equilibrium Al$_8$Mo$_3$ phase, which in turn are decisive to explain the peculiar microstructure formed during demixing.

The four orientations of the Al$_8$Mo$_3$ phase in the D0$_{22}$ matrix (see section 3.3 and Fig. 9) can be explained like in the case of the D0$_{22}$ + D0$_{22}$': In both cases an approximate cube-on-cube orientation relationship is encountered. In the D0$_{22}$ + D0$_{22}$' microstructure the directions having the largest eigenvector of the Aizu strain (see Table 2) are oriented in parallel, whereas the misfits perpendicular to that direction are accommodated by the checkerboard pattern and the rotations around the $\langle 001\rangle_{D0_{22}, D0_{22}'}$. In the D0$_{22}$ + Al$_8$Mo$_3$ microstructure, the EBSD investigations show that the specific $\langle 502\rangle_{Al_8Mo_3}$ direction is parallel to $\langle 001\rangle_{D0_{22}}$ for all four encountered variants. The $\langle 502\rangle_{Al_8Mo_3}$ direction is, again, at least approximately, the direction of the eigenvector with largest eigenvalue. Hence, the parallelism of such directions of largest positive strain already present in the D0$_{22}$ + D0$_{22}$' microstructure is maintained. Due to the lower symmetry of the monoclinic phase, now four different directions are possible. In the D0$_{22}$ + Al$_8$Mo$_3$ microstructure the particles of the latter phase appear to be spherodised and are likely already incoherent with respect to the D0$_{22}$ matrix.

5. Conclusions

A dual-phase microstructure has been encountered in Al-rich as-cast Al–Mo–Ti alloys consisting of a tetragonal D0$_{22}$-like fcc superstructure, corresponding to Mo-substituted Al$_3$Ti and of an orthorhombically distorted variant thereof, called D0$_{22}$'. The latter is most likely a metastable phase. Analysis of the structural character of the D0$_{22}$' phase by powder X-ray diffraction and local composition measurements leads to the following conclusions:

(i) Local composition measurements indicate < 75 at.% Al in the D0$_{22}$ + D0$_{22}$' phase regions as well as higher Mo content in D0$_{22}$' as compared to the coexisting D0$_{22}$ phase.
(ii) Analysis of the lattice parameters of D0$_{22}$' determined by PXRD was performed by means of a strain tensor (*Aizu strain*) quantifying the distortion away from some average fcc structure. Eigenvalues and eigenvectors of this strain tensor resemble those determined from the crystal structures of the stable fcc-based Al–Mo phases, *exp*-Al$_3$Mo and in particular Al$_8$Mo$_3$. Obviously, the substitution of Ti by Mo starting from stable D0$_{22}$-Al$_3$Ti tends to soften the shear modulus ½(C_{11}–C_{12}) (with C_{ij} being the components of the 6 × 6 elastic matrix in Voigt notation and in standard orientation), which gets negative for D0$_{22}$-Al$_3$Mo (≠ experimentally observed *exp*-Al$_3$Mo) according to first-principles calculations also presented. Softness of the corresponding shear is also revealed by characteristically *hkl* dependent microstrain broadening exhibited by both D0$_{22}$ and D0$_{22}$' observed by powder X-ray diffraction.

As evidenced by transmission electron microscopy, selected area electron diffraction, and transmission Kikuchi diffraction, the dual-phase D0$_{22}$ + D0$_{22}$' shows characteristic features:

(iii) The two phases together form a checkerboard microstructure consisting of domains. The different domains have their $\langle 001\rangle_{D0_{22}, D0_{22}'}$ directions parallel and their $[100]/[010]_{D0_{22}, D0_{22}'}$ directions approximately parallel. The approximate $\{110\}_{D0_{22}, D0_{22}'}$ interface boundaries meet in quadruple lines running along $\langle 001\rangle_{D0_{22}, D0_{22}'}$, leading to quasi-1-dimensional rod-like domains for both phases with rectangular/parallelogram cross section. This leads to quite anisotropic domain sizes, which is sub-μm sized perpendicular $\langle 001\rangle_{D0_{22}, D0_{22}'}$ and 10 to several-10-μm sized along $\langle 001\rangle_{D0_{22}, D0_{22}'}$.
(iv) Neglecting a slight metric difference in the $\langle 001\rangle_{D0_{22}, D0_{22}'}$ directions, as implied by the X-ray diffraction data, a (elastic)

strain-free structure can be predicted on the basis of the measured lattice parameters of both phases. These predictions include experimentally observed rotations of the domains along $\langle 001\rangle_{D0_{22},\ D0_{22}'}$: observed alternate (by 90°) orientations of the $D0_{22}$' phase and the two distinct misorientations of the different $D0_{22}$ domains with respect to $D0_{22}$'.

(v) In spite of the predicted strain-free structure, curved grain boundaries observed at the ambient investigation temperatures imply significant stresses at the grain boundaries or at the quadruple lines. This can be explained by minimization of the elastic energy at a high temperature and additional strains introduced additional interdiffusion during cooling or by thermal misfit between the two phases.

(vi) The observed microstructure has likely formed directly during (non-equilibrium) solidification, or by solidification of $D0_{22}$ phase followed by (e.g.) spinodal decomposition during cooling leading to phase separation into Mo-rich ($D0_{22}$') and Ti-rich ($D0_{22}$) regions.

(vii) Upon annealing in the solid state at 1400 °C, the $D0_{22} + D0_{22}$' microstructure tends to decompose under formation of the likely thermodynamically stable Al_8Mo_3 phase, leading still to a microstructure minimizing the strain between the $D0_{22}$ matrix, showing still some features of the dual-phase microstructure, implying its high stability.

The metastable $D0_{22}$' as well as the stable *exp*-Al_3Mo and Al_8Mo_3 phases encountered under equilibrium conditions can be conceived as an extension of the series of $L1_2$, $D0_{23}$, $D0_{22}$ fcc superstructures of early transition metal (approximate) trialuminides Al_3TM. The latter three structures are known to occur with increasing number of electrons per formula unit Al_3TM, especially with *TM* from the group-iii to group-v transition metals. By incorporating now the group-vi elements, an increased number of electrons is introduced leading in $D0_{22}$' to a characteristic orthorhombic distortion away from the tetragonal $D0_{22}$ superstructure, whereas the closely related *exp*-Al_3Mo and Al_8Mo_3 experience additional to the distortion, some monoclinic modification of the long-range ordering.

Declaration of competing interest

The authors declare that they have no known competing financial interests or personal relationships that could have appeared to influence the work reported in this paper.

CRediT authorship contribution statement

A. Leineweber: Conceptualization, Methodology, Formal analysis, Investigation, Resources, Writing - original draft, Visualization, Funding acquisition. **M.J. Kriegel:** Investigation, Writing - review & editing, Investigation, Visualization. **B. Distl:** Investigation, Writing - review & editing, Investigation. **S. Martin:** Methodology, Formal analysis, Investigation, Writing - review & editing, Visualization. **V. Klemm:** Investigation, Writing - review & editing, Investigation. **S.-L. Shang:** Investigation, Formal analysis, Investigation, Writing - review & editing. **Z.-K. Liu:** Resources, Writing - review & editing, Funding acquisition.

Acknowledgements

The authors thank Dipl.-Ing. (FH) A. Leuteritz (TU Bergakademie Freiberg) for preparation of the TEM speciments and M.Sc. A. Treichel for conducting the EPMA measurements. S.L.S. and Z.K.L. acknowledge the financial support from the U.S. National Science Foundation (NSF) via Grant No. CMMI-1825538. First-principles calculations were carried out partially on the resources of the NERSC (National Energy Research Scientific Computing Center) supported by the Office of Science of the U.S. DOE under Contract No. DE-AC02-05CH11231 and partially on the resources of XSEDE (Extreme Science and Engineering Discovery Environment) supported by NSF via Grant No. ACI-1548562.

Appendix. Derivation strain-free interfaces assuming shear transition between $D0_{22}$ and $D0_{22}$'

A version of Eq. (2b) with the basis vectors of the respective unit cells pointing along $\mathbf{e}_1$, $\mathbf{e}_2$ and $\mathbf{e}_3$,

$$\left(\mathbf{a}_{D0_{22}'}\quad \mathbf{b}_{D0_{22}'}\quad \mathbf{c}_{D0_{22}'}\right) = (\mathbf{I}+\boldsymbol{\varepsilon})\left(\mathbf{a}_{D0_{22}}\quad \mathbf{b}_{D0_{22}}\quad \mathbf{c}_{D0_{22}}\right), \tag{A1}$$

allows determining a (symmetric) Bain (transformation/stretch) tensor relating the two structures:

$$\mathbf{B}_1 = \mathbf{I}+\boldsymbol{\varepsilon} = \begin{pmatrix} \frac{a_{D0_{22}'}}{a_{D0_{22}}} & 0 & 0 \\ 0 & \frac{b_{D0_{22}'}}{a_{D0_{22}}} & 0 \\ 0 & 0 & \frac{c_{D0_{22}'}}{c_{D0_{22}}} \end{pmatrix} = \begin{pmatrix} \eta_1 & 0 & 0 \\ 0 & \eta_2 & 0 \\ 0 & 0 & \eta_3 \end{pmatrix}. \tag{A2}$$

Note that presently (comparison of two different phases with definite lattice parameters) $\mathbf{B}_1 - \mathbf{I}$ does not fulfill the restrictions for the spontaneous strain $\boldsymbol{\varepsilon}_{Aizu}$ considered in section 3.1; it now describes the distortion explicitly with respect to the metrics of $D0_{22}$. Adopting now the lattice parameters from the $Al_{73}Mo_{22}Ti_5$ alloy (PXRD data; see Table 3), from which the microstructural observations (Figs. 5–8) have been made, one obtains:

$$\begin{aligned} \mathbf{B}_1 &= \begin{pmatrix} 1.0435 & 0 & 0 \\ 0 & 0.9523 & 0 \\ 0 & 0 & 1.0003 \end{pmatrix} \\ &\approx \begin{pmatrix} 1.0436 & 0 & 0 \\ 0 & 0.9523 & 0 \\ 0 & 0 & 1.0004 \end{pmatrix}. \end{aligned} \tag{A3}$$

Adopting now, however, a unit cell of $D0_{22}$' rotated by 90° around the **c** axis of $D0_{22}$, one obtains a second *correspondence variant* [40,64,65], a term used in martensite theory but also beyond:

$$\mathbf{B}_2 = \mathbf{I}+\boldsymbol{\varepsilon} = \begin{pmatrix} \eta_2 & 0 & 0 \\ 0 & \eta_1 & 0 \\ 0 & 0 & \eta_3 \end{pmatrix}. \tag{A4}$$

If $D0_{22}$' forms from $D0_{22}$ via homogeneous deformation by a deformation gradient tensor **F**, it holds:

$$\left(\mathbf{a}_{D0_{22}'}\quad \mathbf{b}_{D0_{22}'}\quad \mathbf{c}_{D0_{22}'}\right) = \mathbf{F}\left(\mathbf{a}_{D0_{22}}\quad \mathbf{b}_{D0_{22}}\quad \mathbf{c}_{D0_{22}}\right) \tag{A5}$$

where, from now on, the basis vectors are not necessarily oriented along $\mathbf{e}_1$-$\mathbf{e}_3$. In order that **F** complies with an IPS it is necessary to describe it in terms of

$$\mathbf{F} = \mathbf{I} + \mathbf{s}\hat{\mathbf{n}}^T \tag{A6}$$

where **s** is a shift vector and where $\hat{\mathbf{n}}^T$ is the transpose of the unit vector perpendicular to the plane along which the IPS occurs. **s** is

generally not perpendicular to $\hat{\mathbf{n}}$, which allows some volume change ($\mathbf{s}^T\hat{\mathbf{n}} = 0$ implies no volume change; the IPS becomes a simple shear in that case). Note that **F** being an IPS implies that **F** has two linearly independent eigenvectors with eigenvalue 1 perpendicular to $\hat{\mathbf{n}}$.

In order to derive an **F** corresponding to an IPS, it is often expressed in terms of the matrix product

$$\mathbf{F} = \mathbf{RBL}, \tag{A7}$$

where **R** is some rotation matrix (with determinant of +1), where **B** is the Bain strain determined by the crystallography of the respective phases, which can presently assume $\mathbf{B}_1$ and $\mathbf{B}_2$ (see above) and where **L** is a lattice invariant strain (slip or twinning) deforming the new phase inhomogeneously. Such a lattice invariant strain (a simple shear; typically accomplished by slip or twinning) is required to achieve an IPS type for most types of **B**. An IPS with $\mathbf{L} = \mathbf{I}$ simplifying Eq. (A7) towards

$$\mathbf{F} = \mathbf{RB} \tag{A8}$$

is only possible with one eigenvalue of **B** being 1 and the other two eigenvalues being <1 and >1. This condition is, indeed, quite well fulfilled by the present $\mathbf{B}_{1,2}$ matrices (see Eqs. (A3, A4)). The corresponding B_{33} components will be set = 1 from now on (i.e. the minute numerical difference between lengths $c_{D0_{22}'}$ and $c_{D0_{22}}$ resulting from unconstrained Rietveld refinement is neglected). This ensures an eigenvector with eigenvalue 1 along $\mathbf{c}_{D0_{22}}$. A further eigenvector with unit eigenvalue can be achieved by rotation of the deformed structure ($D0_{22}$') around $\mathbf{c}_{D0_{22}}$ about an angle ϕ such that a second eigenvector with eigenvalue = 1 appears. The deformation gradient $\mathbf{F}_1$ holding for the correspondence variant with Bain strain $\mathbf{B}_1$, reads:

$$\mathbf{F}_1 = \mathbf{RB}_1 = \begin{pmatrix} \cos\phi & -\sin\phi & 0 \\ \sin\phi & \cos\phi & 0 \\ 0 & 0 & 1 \end{pmatrix} \mathbf{B}_1 = \begin{pmatrix} \eta_1\cos\phi & -\eta_2\sin\phi & 0 \\ \eta_1\sin\phi & \eta_2\sin\phi & 0 \\ 0 & 0 & 1 \end{pmatrix}. \tag{A9}$$

$\mathbf{F}_1$ has a second unit eigenvector $\hat{\mathbf{r}} = (r_1, r_2, 0)^T$ fulfilling $\mathbf{F}_1\hat{\mathbf{r}} = \hat{\mathbf{r}}$ for specific values of ϕ. These can be determined easiest requiring (following considering only the upper-left four elements in Eq. (A9)):

$$\det\begin{pmatrix} \eta_1\cos\phi - 1 & -\eta_2\sin\phi \\ \eta_1\sin\phi & \eta_2\cos\phi - 1 \end{pmatrix} = 0. \tag{A10}$$

This equation is solved by

$$\cos\phi = \frac{1 + \eta_1\eta_2}{\eta_1 + \eta_2} \tag{A11}$$

corresponding to $\phi = \pm 2.62°$. Adopting the ± values for ϕ, yields $\hat{\mathbf{r}} = (0.7146, \pm 0.6662, 0)^T$, in Cartesian coordinates with basis vectors parallel to the axes of the $D0_{22}$ phase. Together with the eigenvector $(0,0,1)^T$ the two eigenvectors yield $\hat{\mathbf{n}} = (.6995, \mp .7146, 0)^T$ (and equivalently $(-.6995, \pm .7146, 0)^T$). With $\mathbf{B}_2$ instead of $\mathbf{B}_1$, one obtains likewise $\phi = \pm 2.62°$ with $\hat{\mathbf{n}} = (.7146, \pm .6995, 0)^T$ (and $(-.7146, \mp .6995, 0)^T$).

In view of the resulting microstructure it is also convenient to treat the opposite $D0_{22}' \rightarrow D0_{22}$ transformation explicitly. Given an specific orthorhombic $D0_{22}$' phase orientation, there is only one single admissible Bain tensor corresponding to $\mathbf{B}_1^{-1}$ with the diagonal components η_1^{-1}, η_2^{-1} and 1 ($\mathbf{B}_2^{-1}$ applied to the lattice parameters of $D0_{22}$' with $a_{D0_{22}'} > b_{D0_{22}'}$ leads to lattice parameters not complying with those of $D0_{22}$). With the same argument leading to Eq. (A9), a rotation angle ϕ' is sought for fulfilling Eq. (A11) with η_1^{-1}, η_2^{-1} instead of η_1, η_2, yielding analogously $\phi' = \pm 2.62°$. Adopting these angles, one obtains a unit eigenvectors of $\hat{\mathbf{r}}' = (0 \mp .7458, \pm 0.6662, 0)^T$ yielding the habit plane normal $\hat{\mathbf{n}}' = (\pm .6662, .7458, 0)^T$. Note that $\hat{\mathbf{n}}$ and $\hat{\mathbf{n}}'$ refer to the coordinate systems of the individual $D0_{22}$ and $D0_{22}$' grains considered.

The checkerboard microstructure encountered experimentally is depicted in an idealized fashion in Fig. 8 in the main paper. Figure A1 is dedicated to show the compatibility of this microstructure with the derived geometry in more detail. Starting from the $D0_{22}$' grain at the bottom of Figure A1, the four equivalent planes $\{.6662, .7458, 0\}^T$ form the rhomb shape of the grain. Adjacent $D0_{22}$ grains are rotated by $\phi' = +2.62°$ for $\pm(.6662, .7458, 0)^T$ and by $\phi' = -2.62°$ for $\pm(.6662, -.7458, 0)^T$. The orientation of the boundaries with respect to the rotated bases for $D0_{22}$ can be shown to comply with $\{.7146, .6995, 0\}^T$ referring to the axes of the corresponding $D0_{22}$. Four out of the eight $\{.7146, .6995, 0\}^T$ can be used to make up the square shapes of the $D0_{22}$ grains.

Coming now to the upper $D0_{22}$' rhomb in Figure A1. This rhomb is rotated by 90° with respect to the other rhomb around the common $001_{D0_{22}/D0_{22}'}$ direction, this is inscribed by the same $\{.6662, .7458, 0\}^T$ referring to the rotated axes. The same orientations $D0_{22}$ grain orientations can be achieved via the specific subsets of the boundaries as they can be derived from the lower rhomb.

The resulting two orientations can be conceived as correspondence variants associated with $\mathbf{B}_1$ and $\mathbf{B}_2$ above, if derived from $D0_{22}$. Note that if $D0_{22}$' would be formed within a $D0_{22}$ matrix the two $D0_{22}$' correspondence variants lead with two rotations and associated habit planes to four different habit plane variants. The present microstructure model actually follows the same local features, leading, however, to two $D0_{22}$ and $D0_{22}$' orientations.

References

[1] H. Clemens, S. Mayer, Design, processing, microstructure, properties, and applications of advanced intermetallic TiAl alloys, Adv. Eng. Mater. 15 (2013) 191–215, https://doi.org/10.1002/adem.201200231.

[2] K.S. Kumar, Ternary intermetallics in aluminium–refractory metal-X systems (X = V, Cr, Mn, Fe, Co, Ni, Cu, Zn), Int. Mater. Rev. 35 (1990) 293–327, https://doi.org/10.1179/095066090790324037.

[3] Y. Nakayama, M. Mabuchi, Formation of ternary $L1_2$ compounds in Al_3Ti-base alloys, Intermetallics 1 (1993) 41–48, https://doi.org/10.1016/0966-9795(93)90020-V.

[4] J.F. Cannon, H.T. Hall, Effect of high pressure on the crystal structures of lanthanide trialumindes, J. Less Common. Met. 40 (1975) 313–328, https://doi.org/10.1016/0022-5088(75)90076-4.

[5] G. Brauer, Über die Kristallstruktur von $TiAl_3$, $NbAl_3$, $TaAl_3$, und $ZrAl_3$, Z. Anorg. Allg. Chem. 242 (1942) 1–22, https://doi.org/10.1002/zaac.19392420101.

[6] A.E. Dwight, J.W. Downey, R.A. Conner Jr., Some AB_3 compounds of the transition metals, Acta Crystallogr. 14 (1961) 75–76, https://doi.org/10.1107/S0365110X61000255.

[7] C. Colinet, A. Pasturel, Ab initio calculation of the formation energies of $L1_2$, $D0_{22}$, $D0_{23}$ and one dimensional long period structures in $TiAl_3$ compound, Intermetallics 10 (2002) 751–764, https://doi.org/10.1016/S0966-9795(02)00054-7.

[8] G. Ghosh, M. Asta, First-principles calculation of structural energetics of Al-TM (TM = Ti, Zr, Hf) intermetallics, Acta Mater. 53 (2005) 3225–3252, https://doi.org/10.1016/j.actamat.2005.03.028.

[9] C.M. Fang, Z. Fan, An ab initio study on stacking and stability of $TiAl_3$ phases, Comput. Mater. Sci. 153 (2018) 309–314, https://doi.org/10.1016/j.commatsci.2018.07.011.

[10] A. Raman, K. Schubert, Über den Aufbau einiger zu $TiAl_3$ verwandter Legierungsreihen. II. Untersuchungen in einigen T-Al-Si und T^4…^{6}-In Systemen, Z. Metallkde 56 (1965) 44–52.

[11] F.J.J. van Loo, G.D. Rieck, Diffusion in the titanium-aluminium system-I. Interdiffusion between solid Al and Ti or Ti-Al alloys, Acta Metall. 21 (1973) 61–71, https://doi.org/10.1016/0001-6160(73)90220-4.

[12] H. Boller, H. Nowotny, A. Wittmann, Die Kristallstruktur einiger Hafnium-haltiger phasen, Monatshefte Chem. 91 (1960) 1174–1184, https://doi.org/10.1007/BF00899845.

[13] G. Brauer, Konstitution der Aluminium-Vanadium-Verbindung VAl_3, Z. Elektrochem. 49 (1943) 208–210, https://doi.org/10.1002/bbpc.19430490407.

[14] M.E. Eberhart, K.S. Kumar, J.M. MacLaren, An electronic model for the $D0_{22}$ to $L1_2$ transformation of the group IVA trialuminides, Philos. Mag. B 61 (1990) 943–956, https://doi.org/10.1080/13642819008207854.

[15] J.-H. Xu, A.J. Freeman, Band filling and structural stability of cubic trialuminides: YAl_3, $ZrAl_3$, and $NbAl_3$, Phys. Rev. B 40 (1989) 11927–11930, https://doi.org/10.1103/PhysRevB.40.11927.

[16] A.T. Paxton, D.G. Pettifor, Al_3Ru – a ductile trialuminide? Scripta Met. Mater. 26 (1992) 529–533, https://doi.org/10.1016/0956-716X(92)90278-M.

[17] C.L. Condron, G.J. Miller, J.D. Strand, S.L. Budko, P.C. Canfield, A new look at bonding in Trialuminides: reinvestigation of $TaAl_3$, Inorg. Chem. 42 (2003) 8371–8376, https://doi.org/10.1021/ic034927m.

[18] V.J. Yanello, D.C. Fredrickson, Generality of the 18–n rule: intermetallic structural chemistry explained through isolobal analogies to transition metal complexes, Inorg. Chem. 54 (2015) 11385–11398, https://doi.org/10.1021/acs.inorgchem.5b02016.

[19] J.B. Forsyth, G. Gran, The structure of the intermetallic phase γ(Mo–Al)–Mo_3Al_8, Acta Crystallogr. 15 (1962) 100–104, https://doi.org/10.1107/S0365110X62000304.

[20] M. Pötzschke, K. Schubert, Zum Aufbau einiger zu T(4)-B(3) homologer und quasihomologer Systeme.II Die Systeme Titan-Aluminium, Zirkonium-Aluminium, Hafnium-Aluminium, Molybdän-Aluminium, und einige ternäre System, Z. Metallkde 53 (1962) 548–561.

[21] J.C. Schuster, H. Ipser, The Al-Al_8Mo_3 section of the binary system Aluminum-molybdenum, Metall. Trans. A 22 A (1991) 1729–1738, https://doi.org/10.1007/BF02646496.

[22] S. Enzo, R. Frattini, P. Canton, M. Monagheddu, F. Delogu, Neutron diffraction study of mechanically alloyed and in situ annealed $Al_{75}Mo_{25}$ powders, J. Appl. Phys. 87 (2000) 2753–2759, https://doi.org/10.1063/1.372251.

[23] M.J. Kriegel, O. Fabrichnaya, M. Conrad, V. Klemm, J. Freudenberger, A. Leineweber, High temperature phase equilibria in the Ti-poor part of the Al–Mo–Ti system, J. Alloy. Comp. 706 (2017) 616–628, https://doi.org/10.1016/j.jallcom.2017.02.205.

[24] X.M. Huang, L.L. Zhu, G.M. Cai, H.S. Liu, Z.P. Jin, Experimental investigation of phase equilibria in the Ti–Al–Mo ternary system, J. Mater. Sci. 52 (2017) 2270–2284, https://doi.org/10.1007/s10853-016-0520-5.

[25] V.T. Witusiewicz, A.A. Bondar, U. Hecht, O.M. Stryzhyboroda, N.I. Tsyganenko, V.M. Voblikov, V.M. Petyukh, T. Ya Velikanova, Thermodynamic re-modelling of the ternary Al–Mo–Ti system based on novel experimental data, J. Alloy. Comp. 749 (2018) 1071–1091, https://doi.org/10.1016/j.jallcom.2018.03.283.

[26] M.J. Kriegel, A. Walnsch, B. Distl, O. Fabrichnaya, J. Freudenberger, A. Leineweber, The ternary Al–Mo–Ti system revisited: phase equilibria of $Al_{63}(Mo,Ti)_{37}$, J. Alloy. Comp. 811 (2019), https://doi.org/10.1016/j.jallcom.2019.152055, 152055-1-10.

[27] TOPAS V5.0, Bruker AXS, Karlsruhe, Germany, 2014.

[28] R.E. Dinnebier, A. Leineweber, J.S.O. Evans, Rietveld Refinement: Practical Powder Diffraction Pattern Analysis Using TOPAS, De Gruyter, Berlin, 2019.

[29] P. Thompson, D.E. Cox, J.B. Hastings, Rietveld refinement of Debye-Scherrer synchrotron X-ray data from Al_2O_3, J. Appl. Crystallogr. 20 (1987) 79–83, https://doi.org/10.1107/S0021889887087090.

[30] A. Leineweber, Understanding anisotropic microstrain broadening in Rietveld refinement, Z. Kristallogr. 226 (2011) 905–923, https://doi.org/10.1524/zkri.2011.1413.

[31] G. Kresse, J. Furthmüller, Efficient iterative schemes for ab initio total-energy calculations using a plane-wave basis set, Phys. Rev. B. 54 (1996) 11169–11186, https://doi.org/10.1103/PhysRevB.54.11169.

[32] G. Kresse, D. Joubert, From ultrasoft pseudopotentials to the projector augmented-wave method, Phys. Rev. B. 59 (1999) 1758–1775, https://doi.org/10.1103/PhysRevB.59.1758.

[33] J.P. Perdew, K. Burke, M. Ernzerhof, Generalized gradient approximation made simple, Phys. Rev. Lett. 77 (1996) 3865–3868, https://doi.org/10.1103/PhysRevLett.77.3865.

[34] M. Methfessel, A.T. Paxton, High-precision sampling for Brillouin-zone integration in metals, Phys. Rev. B. 40 (1989) 3616–3621, https://doi.org/10.1103/PhysRevB.40.3616.

[35] P.E. Blöchl, O. Jepsen, O.K. Andersen, Improved tetrahedron method for Brillouin-zone integrations, Phys. Rev. B. 49 (1994) 16223–16233, https://doi.org/10.1103/PhysRevB.49.16223.

[36] S.-L. Shang, Y. Wang, D. Kim, Z.-K. Liu, First-principles thermodynamics from phonon and Debye model: application to Ni and Ni_3Al, Comput. Mater. Sci. 47 (2010) 1040–1048, https://doi.org/10.1016/j.commatsci.2009.12.006.

[37] S.-L. Shang, Y. Wang, T.J. Anderson, Z.-K. Liu, Achieving accurate energetics beyond (semi-)local density functional theory: illustrated with transition metal disulfides, Cu_2ZnSnS_4, and Na_3PS_4 related semiconductors, Phys. Rev. Mater. 3 (2019), 015401, https://doi.org/10.1103/PhysRevMaterials.3.015401.

[38] S.L. Shang, Y. Wang, Z.K. Liu, First-principles elastic constants of α- and θ-Al_2O_3, Appl. Phys. Lett. 90 (2007) 101909, https://doi.org/10.1063/1.2711762.

[39] S.L. Shang, D.E. Kim, C.L. Zacherl, Y. Wang, Y. Du, Z.K. Liu, Effects of alloying elements and temperature on the elastic properties of dilute Ni-base superalloys from first-principles calculations, J. Appl. Phys. 112 (2012), 053515, https://doi.org/10.1063/1.4749406.

[40] K. Bhattacharya, Microstructure of Martensite: Why it Forms and How it Gives Rise to the Shape-Memory Effect, Oxford University Press Inc., New York, USA, 2003, ISBN 9780198509349.

[41] C. Giacovazzo, Fundamentals of Crystallography, third ed., Oxford University Press Inc., New York, USA, 2011, ISBN 9780199573660.

[42] A. Leineweber, T. Hickel, B. Azimi-Manavi, S. Maisel, Crystal structures of Fe_4C vs. Fe_4N analysed by DFT calculations: fcc-based interstitial superstructures explored, Acta Mater. 140 (2017) 433–442, https://doi.org/10.1016/j.actamat.2017.08.059.

[43] C. Wieser, A. Walnsch, W. Hügel, A. Leineweber, The monoclinic distortion of η′-Cu_6Sn_5, J. Alloy. Comp. 794 (2019) 491–500, https://doi.org/10.1016/j.jallcom.2019.04.265.

[44] K. Aizu, Determination of the state parameters and formulation of spontaneous strain for ferroelastics, J. Phys. Soc. Japan 28 (1970) 706–716, https://doi.org/10.1143/JPSJ.28.706.

[45] A. Leineweber, Reflection-splitting induced microstrain broadening, Powder Diffr. 32 (2017) S35–S39, https://doi.org/10.1017/S0885715617000665.

[46] P. Norby, A. Norlund Christensen, Preparation and structure of Al_3Ti, Acta Chem. Scand. 40A (1986) 157–159, https://doi.org/10.3891/acta.chem.scand.40a-0157.

[47] Y. Ma, C. Romming, B. Lebech, J. Gjonnes, J. Tafto, Structure refinement of Al_3Zr, using single crystal X-ray diffraction powder diffraction and CBED, Acta Crystallogr. B 48 (1992) 11–16, https://doi.org/10.1107/S0108768191010467.

[48] J.L. Jorda, R. Flückiger, J. Muller, A new metallurgical investigation of the niobium-aluminium system, J. Less Common. Met. 75 (1980) 227–239, https://doi.org/10.1016/0022-5088(80)90120-4.

[49] A. Jain, S.P. Ong, G. Hautier, W. Chen, W.D. Richards, S. Dacek, S. Cholia, D. Gunter, D. Skinner, G. Ceder, K.A. Persson, Commentary: the Materials Project: a materials genome approach to accelerating materials innovation, Apl. Mater. 1 (2013) 1–11, https://doi.org/10.1063/1.4812323, 011002.

[50] T. Hahn (Ed.), International Tables for Crystallography, fifth ed. A, Springer, Dordrecht, The Netherlands, 2005 corrected reprint.

[51] W.A. Dollase, Correction of intensities for preferred orientation in powder diffractometry: application of the March model, J. Appl. Crystallogr. 19 (1986) 267–272, https://doi.org/10.1107/S0021889886089458.

[52] M. Jahnátek, M. Krajci, J. Hafner, Interatomic bonding, elastic properties, and ideal strength of transition metal aluminides: a case study for $Al_3(V,Ti)$, Phys. Rev. B 71 (2005), https://doi.org/10.1103/PhysRevB.71.024101, 024101-16.

[53] A. Leineweber, R.E. Dinnebier, Anisotropic microstrain broadening of minium, Pb_3O_4, in a high-pressure cell: interpretation of line-width parameters in terms of stress variations, J. Appl. Crystallogr. 43 (2010) 17–26, https://doi.org/10.1107/S002188980904758X.

[54] Z. Chen, I.P. Jones, C.J. Small, The structure of the alloy Ti–50Al–15Mo between 800°C and 1400°C, Acta Mater. 45 (1997) 3801–3815, https://doi.org/10.1016/S1359-6454(97)00049-9.

[55] J.-M. Joubert, R. Cerny, M. Latroche, A. Percheron-Guégan, K. Yvon, Site occupancies in the battery electrode material $LaNi_{3.55}Mn_{0.4}Al_{0.3}Co_{0.75}$ as determined by multiwavelength synchrotron powder diffraction, J. Appl. Crystallogr. 31 (1998) 327–332, https://doi.org/10.1107/S0021889897010911.

[56] M.J. Kriegel, D. Pavlyuchkov, D.M. Cupid, O. Fabrichnaya, D. Heger, D. Rafaja, H.J. Seifert, Phase equilibria at 1473 K in the ternary Al–Cr–Ti system, J. Alloy. Comp. 550 (2013) 519–525, https://doi.org/10.1016/j.jallcom.2012.10.123.

[57] C.R. Hunt jr., A. Raman, Alloy chemistry of σ(βU)-related phases, Z. Metallkde 59 (1968) 701–707.

[58] M.-X. Zhang, P.M. Kelly, Crystallographic features of phase transformations in solids, Prog. Mater. Sci. 54 (2009) 1101–1170, https://doi.org/10.1016/j.pmatsci.2009.06.001.

[59] Y. Ni, A.G. Khachaturyan, From chessboard tweed to chessboard nanowire structure during pseudospinodal decomposition, Nat. Mater. 8 (2009) 410–414, https://doi.org/10.1038/nmat2431.

[60] C. Leroux, A. Liseau, G. Broddin, G. Van Tendeloo, Electron microscopy study of the coherent two-phase mixtures $L1_0 + L1_2$ in Co-Pt alloys, Philos. Mag. B 64 (1991) 57–82, https://doi.org/10.1080/13642819108207603.

[61] M. Takeyama, M. Kikuchi, Eutectoid transformations accompanied by ordering, Intermetallics 6 (1998) 573–578, https://doi.org/10.1016/S0966-9795(98)00041-7.

[62] A. Suzuki, H. Kojima, T. Matsuo, M. Takeyama, Alloying effect on stability of multi-variant structure of Ni_3V at elevated temperatures, Intermetallics 12 (2004) 969–975, https://doi.org/10.1016/j.intermet.2004.02.028.

[63] L.A. Bendersky, W.J. Boettinger, Phase Transformations in the (Ti, $Nb)_3Al$ section of the Ti-Al-Nb System–II. Experimental TEM study of microstructures, Acta Metall. Mater. 42 (1994) 2337–2352, https://doi.org/10.1016/0956-7151(94)90312-3.

[64] Y. Gao, R. Shi, J.-F. Nie, S.A. Dregia, Y. Wang, Group theory description of transformation pathway degeneracy in structural phase transformations, Acta Mater. 109 (2016) 353–363, https://doi.org/10.1016/j.actamat.2016.01.027.

[65] C. Cayron, The transformation matrices (distortion,orientation, correspondence), their continuous forms and their variants, Acta Crystallogr. A 75 (2019) 411–437, https://doi.org/10.1107/S205327331900038X.